Geosci. Model Dev. Discuss., 6, 59–119, 2013
www.geosci-model-dev-discuss.net/6/59/2013/
doi:10.5194/gmdd-6-59-2013

Geoscientific
Model Development
Discussions

The ICON-1.2 hydrostatic atmospheric dynamical core on triangular grids – Part 1: Formulation and performance of the baseline version

H. Wan[1,4,*], M. A. Giorgetta[1], G. Zängl[2], M. Restelli[3], D. Majewski[2], L. Bonaventura[3], K. Fröhlich[2,1], D. Reinert[2], P. Rípodas[2], and L. Kornblueh[1]

[1]Max Planck Institute for Meteorology, Hamburg, Germany
[2]German Weather Service, Offenbach am Main, Germany
[3]MOX – Department of Mathematics F. Brioschi, Politecnico di Milano, Milan, Italy
[4]International Max Planck Research School on Earth System Modelling, Hamburg, Germany
[*]now at: Pacific Northwest National Laboratory, Richland, WA, USA

Received: 27 December 2012 – Accepted: 4 January 2013 – Published: 17 January 2013

Correspondence to: H. Wan (hui.wan@zmaw.de)

Published by Copernicus Publications on behalf of the European Geosciences Union.

Abstract

A hydrostatic atmospheric dynamical core is developed for the purpose of global climate modelling. The model applies finite-difference methods to discretize the primitive equations on spherical icosahedral grids, using C-type staggering with triangles as control volumes for mass. This paper documents the numerical methods employed in the baseline version of the model, discusses their properties, and presents results from various idealized test cases. The evaluation shows that the new dynamical core is able to correctly represent the evolution of baroclinic eddies in the atmosphere as well as their role in heat and momentum transport. The simulations compare well with the reference solutions, and show a clear trend of convergence as the horizontal resolution increases. First results from two aqua-planet simulations are also presented, in which the equatorial wave spectra derived from tropical precipitation agree well with those simulated by a spectral transform model. The new dynamical core thus provides a good basis for further model development. Certain aspects of the model formulation that need further investigation and improvement are also pointed out.

1 Introduction

In the development of general circulation models (GCMs) for the purpose of numerical weather prediction (NWP) and climate research, one of the essential tasks is to design numerically accurate, robust, and computationally efficient algorithms to solve the adiabatic fluid dynamics equations that govern the atmospheric motions. This component of a GCM, commonly referred to as the dynamical core, provides meteorological background for and interacts with large scale tracer transport as well as diabatic processes like radiative heating/cooling and cumulus convection. Numerical properties of the dynamical core play an important role in determining the behavior of an atmospheric model.

Until the 1990's, spectral transform methods applied on latitude-longitude grids had been a popular choice for dynamical cores at many weather forecasting services and climate research centers, due to the excellent accuracy and efficiency in approximating wave propagation in a spherical domain without lateral boundaries. As the resolution of global models starts to increase toward cloud resolving scales, and as the application scope extends to include chemical and biogeochemical processes, other numerical features such as conservation properties and tracer-and-air-mass consistency become increasingly desirable or even crucial. Hence, grid point methods have been considered again as an alternative to the spectral transform method. The idea of using grid point based methods on geodesic grids, originally proposed in the late 1960's (Williamson, 1968; Sadourny et al., 1968), has been revisited to avoid the polar singularities of global latitude-longitude grids. Modern numerical techniques such as high-order continuous and discontinuous Galerkin methods have also been investigated. Examples include the work by Heikes and Randall (1995), Ringler and Randall (2002), Majewski et al. (2002), Giraldo and Rosmond (2004), Tomita and Satoh (2004), to name but a few. A general overview of the historical development and recent advances in this research area can be found in Bonaventura et al. (2012), along with a more complete list of references. At the Max Planck Institute for Meteorology (MPI-M) and the German Weather Service, a collaboration was initiated in 2001 to develop high-resolution nonhydrostatic models with the capability of static local zooming, to be used for operational weather prediction as well as for climate research. Previous experiences had underlined the importance of conservation of air mass and atmospheric constituents, as well as the advantages of developing atmosphere and ocean models in the same framework. Based on these considerations, the two institutions chose to employ finite difference/finite volume methods on icosahedral grids with C-type staggering, giving the name "ICON" (**ICO**sahedral **N**onhydrostatic dynamical cores) to the joint project.

Based on the ICON shallow water model developed by Bonaventura and Ringler (2005) and further tested by Rípodas et al. (2009), a hydrostatic atmospheric dynamical core (hereafter referred to as the ICOHDC) is established in this work. This is an intermediate step towards the ultimate goal (i.e. a nonhydrostatic core) of the ICON project. At MPI-M rich experience has been accumulated in the past decades with the ECHAM model series which employ the hydrostatic assumption (Roeckner et al., 1992, 1996, 2006; Giorgetta et al., 2012). In order to assess potential benefits or drawbacks of using icosahedral grids and the proposed finite difference discretization in an isolated manner, i.e. to separate them from other aspects such as choice of governing equations and dynamics-physics interaction, the hydrostatic dynamical core we describe here has been developed and tested using the same governing equations as in ECHAM. Again to facilitate testing and understanding, the first version of the ICOHDC uses the same vertical discretization and time stepping method as in the spectral transform dynamical core of ECHAM. This baseline version of the new dynamical core is the focus of the present paper. The numerical formulation is described, and its performance evaluated in various idealized test cases. For the purpose of achieving the consistency between tracer and air mass, other time stepping schemes have been investigated. These alternatives, together with additional investigations in the choice of the horizontal grid optimization and spatial discretization, are discussed in a companion paper.

The remainder of this paper is organized as follows: Sects. 2 and 3 present the governing equations and the computational mesh used in the ICOHDC; Sects. 4 and 5 discuss the discrete formulation; Sects. 6 and 7 evaluate the performance of the dynamical core in idealized test cases. Conclusions are summarized in Sect. 8.

2 Governing equations

The governing equations solved by the hydrostatic dynamical core are the primitive equations in velocity-temperature form. A generic pressure-based terrain-following vertical coordinate η is used, the value of which ranges from 0 at the top of the model to 1 at the Earth's surface. The pressure value at the model top is set to 0 hPa to include the total mass of the atmosphere. The prognostic equations of our model read

$$\frac{\partial \boldsymbol{v}}{\partial t} = -(f+\zeta)\,\boldsymbol{k}\times\boldsymbol{v} - \nabla K - \dot{\eta}\frac{\partial p}{\partial \eta}\frac{\partial \boldsymbol{v}}{\partial p} - \frac{R_d T}{p}\nabla p - \nabla \Phi \tag{1}$$

$$\begin{aligned}\frac{\partial T}{\partial t} &= -\boldsymbol{v}\cdot\nabla T - \dot{\eta}\frac{\partial p}{\partial \eta}\frac{\partial T}{\partial p}\\ &\quad + \frac{1}{C_p}\left[\frac{R_d T}{p}\boldsymbol{v}\cdot\nabla p + \frac{R_d T}{p}\left(\frac{\partial p}{\partial t} + \dot{\eta}\frac{\partial p}{\partial \eta}\right)\right]\end{aligned} \tag{2}$$

$$\frac{\partial p_\mathrm{s}}{\partial t} = -\int_0^1 \nabla\cdot\left(\boldsymbol{v}\frac{\partial p}{\partial \eta}\right)\mathrm{d}\eta. \tag{3}$$

They are complemented by two diagnostic equations

$$\dot{\eta}\frac{\partial p}{\partial \eta} = -\int_0^\eta \nabla\cdot\left(\boldsymbol{v}\frac{\partial p}{\partial \eta}\right)\mathrm{d}\eta - \frac{\partial p}{\partial p_\mathrm{s}}\frac{\partial p_\mathrm{s}}{\partial t} \tag{4}$$

$$\Phi = -\int_0^\eta R_d T \ln p\, \mathrm{d}\eta. \tag{5}$$

Here, $\boldsymbol{v}$ stands for the horizontal wind vector, ∇ denotes the horizontal gradient, and $\boldsymbol{k}$ is the local unit vector pointing to the upward direction. $\zeta = (\nabla\times\boldsymbol{v})\cdot\boldsymbol{k}$ denotes the vertical component of the relative vorticity. K is the kinetic energy per unit mass, $K = |\boldsymbol{v}|^2/2$. Φ is the geopotential. $\dot{\eta} = \mathrm{d}\eta/\mathrm{d}t$ stands for the material derivative of η. All the other symbols have their conventional meanings.

Title Page
Abstract | Introduction
Conclusions | References
Tables | Figures
◂◂ | ▸▸
◂ | ▸
Back | Close
Full Screen / Esc
Printer-friendly Version
Interactive Discussion

3 Computational mesh

The horizontal grid generation algorithm used here starts from projecting a regular icosahedron onto the sphere, with two of the twelve vertices coinciding with the North and South Poles. The other five vertices in each hemisphere are located along the latitude circle of 26.6° N/S with equal longitude intervals of 72°. The second step of grid generation is to divide each great circle arc of the projected icosahedron into n_r arcs of equal length, and each icosahedron face into n_r^2 small triangles, as described by Sadourny et al. (1968). This is referred to as the root division. The resulting mesh is designated as the grid level 0. Further mesh refinement is achieved by bisecting each spherical triangle edge and connecting the midpoints by great circle arcs, yielding four small cells for each parent triangle. In our terminology, a root division of the original spherical icosahedron edge into n_r arcs followed by n_b recursive edge bisections leads to the "Rn_rBn_b grid".

From grid level 0 onwards, only the twelve icosahedron vertices are surrounded by five triangles (they are thus also referred to as the pentagon points), while the other vertices are surrounded by six cells. This introduces irregularity into the grid, resulting in inequality in cell areas and edge lengths. Triangles closest to the pentagon points feature the most severe deformation. At each grid level, the algorithm of Tomita et al. (2001) is applied to slightly relocate the vertices, so as to ensure smooth transition of geometric properties. Table 1 shows the properties of various grids.

Like in Bonaventura and Ringler (2005, hereafter referred to as BR05), C-staggering is applied to the triangular cells by placing mass and temperature at triangle circumcenters. This particular choice of cell center (as opposed to, e.g. barycenter) results in the property that the arc connecting two neighboring mass points is orthogonal to and bisects the shared triangle edge. These bisection points are used as velocity points, at which the component of horizontal wind perpendicular to the edge (denoted by v_n in this paper, cf. Fig. 1) is predicted using Eq. (1). In the vertical, the widely used hybrid p-σ coordinate of Simmons and Strüfing (1981) ("coordinate 4" in their report) is employed. The staggering follows Lorenz (1960), meaning that the horizontal wind and temperature are carried at "full levels" representing layer-mean values, while the vertical velocity is diagnosed at "half levels" (i.e. layer interfaces, cf. Fig. 1). The vertical grid is identical to that used in the ECHAM models (cf., e.g. Roeckner et al., 2006).

4 C-grid discretization

In this section we briefly describe the C-grid discretization inherited from the ICON shallow water model of BR05, then present an analysis of its properties.

4.1 Basic operators

BR05 established a spatial discretization method for solving the shallow water equations on the spherical triangular grid described in the previous section. This method forms the basis for the hydrostatic model discussed here. Their discretization concept is a mimetic finite difference scheme consisting of the following elements:

- The discrete model predicts the normal component of the horizontal wind v_n with respect to triangle edges. The tangential component v_τ, needed for the vorticity flux term in the momentum equation, is reconstructed from the normal components using vector radial basis functions (cf. references in Sect. 5.2).

- Horizontal derivatives are represented by four discrete operators. The divergence operator $\mathrm{div}(\boldsymbol{v})$ applies the Gauss theorem on each triangular control volume to approximate the spatially averaged divergence over that cell (Fig. 2a). The curl operator $\mathrm{curl}(\boldsymbol{v})$ uses the Stokes' theorem to approximate the vertical component of the relative vorticity averaged over a dual (hexagonal or pentagonal) cell centered at a triangle vertex and bounded by arcs connecting the centers of all triangles sharing the vertex (Fig. 2a). The directional derivative of a scalar field at the midpoint of a triangle edge in the normal direction, $\mathrm{grad}_n(\cdot)$, is approximated by a straightforward finite-difference discretization involving two cell centers, and referred to as the (normal) gradient operator (Fig. 2b). The horizontal derivative tangential to the edge, $\mathrm{grad}_\tau(\cdot)$, is also defined at the edge midpoint, approximated by a central difference using values at the two ends of the edge (Fig. 2b). The mathematical formulations of the four operators are given by Eqs. (4), (5), (7), and (8) in BR05.

- Higher order spatial derivatives (Laplacian and hyper-Laplacian) are constructed from the four basic operators outlined above (see, e.g. Eq. 14 in Sect. 4.3). These derivatives are needed, for example, in semi-implicit time stepping schemes and for horizontal diffusion.

This discretization scheme is conceptually the same as the widely used C-type discretization on quadrilateral grids. The basic operators are simple, but nevertheless have nice properties. For example the divergence operator per construction makes it straightforward to achieve mass conservation, while the curl operator guarantees that the global integral of the relative vorticity vanishes. The divergence and gradient operators are mimetic in the sense that the rule of integration by parts has a counterpart in the discrete model (cf. Eqs. 9 and 10 in BR05), a desirable property for achieving conservation properties. The basic operators are also highly localized (i.e. defined on small stencils), which is beneficial in massively parallel computing.

However, a question remains whether the good properties of the quadrilateral C-grids in terms of the faithful representation of inertia-gravity waves are inherited by the triangular C-grid without limitation. For the hexagonal/pentagonal grids (which can been viewed as the dual meshes of the triangular grids), the wave dispersion analysis in Ničković et al. (2002) revealed that discretization approaches using C-staggering could produce spurious geostrophic modes. A technique to avoid such modes on the hexagonal/pentagonal meshes was proposed in Thuburn (2008) and further developed in (Thuburn et al., 2009). On the triangular C-grids, spurious modes have also been noticed (e.g. Le Roux et al., 2007; Danilov, 2010). Some recent articles discussed this issue by analyzing the linearized shallow water equations and the representation of vector fields in a trivariate coordinate system (Danilov, 2010; Gassmann, 2011). Here, we take a different perspective and use truncation error analysis to show that the divergence operator on the triangular C-grid described above inherently produces grid-scale checkerboard error patterns. The same analysis leads to a proposal for estimating the specific amount of numerical hyper-diffusion necessary to reduce the impact of these systematic errors on numerical simulations.

4.2 Truncation error analysis

To focus on the triangular geometry and the C-staggering, we carry out the analysis on a planar grid consisting of equilateral triangles of edge length l. We associate a local Cartesian coordinate to each cell with the origin located at the triangle center and the x-axis parallel to one edge. We then denote the normal outward unit vector at edge midpoints by $\boldsymbol{n}_j$ where $j \in [1,3]$ is the edge index. A label δ is assigned to each cell to denote its orientation, with values of 0 and 1 for upward- and downward-pointing triangles, respectively. Thus, the three neighboring cells sharing edges with an upward-pointing triangle are downward-pointing, and vice versa. In the truncation error calculation, a downward-pointing triangle is understood as the image of the corresponding upward-pointing triangle mirrored at the x-axis (Fig. 3). For a generic vector field $\boldsymbol{v}$ differentiable to a sufficiently high order, we denote its components in the x and y directions by u and v, respectively. Applying the discrete divergence operator pointwise values of the vector field known at edge midpoints, denoted as $\boldsymbol{v}_j$, the 2-D Taylor expansion yields

$$\mathrm{div}(\boldsymbol{v}) = \left(\frac{\sqrt{3}\,l^2}{4}\right)^{-1} l \sum_{j=1}^{3} \boldsymbol{v}_j \cdot \boldsymbol{n}_j \tag{6}$$

$$= (\nabla\cdot\boldsymbol{v})_o + (-1)^{\delta}\, l\, H(\boldsymbol{v})_o + \frac{l^2}{96}\left[\nabla^2(\nabla\cdot\boldsymbol{v})\right]_o + (-1)^{\delta}\, l^3 F(\boldsymbol{v})_o + \mathcal{O}(l^4). \tag{7}$$

Here the subscript o denotes the function evaluation at the triangle center. The functions H and F read

$$H(\boldsymbol{v}) = \frac{\sqrt{3}}{24}\left(2\frac{\partial^2 u}{\partial x \partial y} + \frac{\partial^2 v}{\partial x^2} - \frac{\partial^2 v}{\partial y^2}\right), \tag{8}$$

$$F(\boldsymbol{v}) = \frac{\sqrt{3}}{2^9 3^3}\left(12\frac{\partial^4 u}{\partial x^3 \partial y} + 2\frac{\partial^4 u}{\partial x \partial y^3} + 3\frac{\partial^4 v}{\partial x^4} + 6\frac{\partial^4 v}{\partial x^2 \partial y^2} - 5\frac{\partial^4 v}{\partial y^4}\right). \tag{9}$$

Equation (7) indicates that the discrete divergence operator applied to pointwise values of $\boldsymbol{v}$ is a first-order approximation of the divergence at the triangle center. More importantly, the first-order error term changes sign from an upward-pointing triangle to a downward-pointing one, which results in a checkerboard error pattern.

In a finite-volume perspective, the divergence computed by the Gauss theorem should be interpreted as cell average rather than a pointwise value. However, it is worth noting that, in an equilateral triangle, the cell-center value can be viewed as a second-order approximation of the cell average. Therefore, the first order error term in Eq. (7) will also be present in the approximation of the cell average. Indeed, it is not difficult to check that

$$\operatorname{div}(\boldsymbol{v}) = \overline{\overline{(\nabla \cdot \boldsymbol{v})}}^{c} + (-1)^{\delta}\, l\, H(\boldsymbol{v})_o - \frac{l^2}{96}\left[\nabla^2(\nabla \cdot \boldsymbol{v})\right]_o + \mathcal{O}(l^3) \tag{10}$$

where $\overline{\overline{()}}^{c}$ stands for cell average. The leading error remains first order and also features a checkerboard pattern. In order to check empirically the impact of Eq. (10), numerical calculations have been performed using the vector field

$$\begin{cases} u(x,y) &= \dfrac{1}{4}\sqrt{\dfrac{105}{2\pi}}\cos 2x \cos^2 y \sin y\,, \\ v(x,y) &= -\dfrac{1}{2}\sqrt{\dfrac{15}{2\pi}}\cos x \cos y \sin y\,, \end{cases} \tag{11}$$

the divergence of which reads

$$\nabla \cdot \boldsymbol{v} = \frac{-1}{2\sqrt{2\pi}} \left(\sqrt{105}\sin 2x \cos^2 y \sin y + \sqrt{15}\cos x \cos 2y \right). \tag{12}$$

The discrete divergence is calculated by first evaluating Eq. (11) at edge centers and then applying operator (6). Numerical errors are calculated against the cell average given in Appendix A. Figure 4 shows the spatial distribution of the error and the convergence with respect to resolution. These results confirm the error analysis in Eq. (10).

It could also be remarked that, if the operand of the divergence operator is interpreted as the average along the edge rather than the point value at the edge center, then the Gauss theorem will give the exact cell-averaged divergence without any error. However, it should be noted that in a C-grid discretization, the divergence operator is typically not applied to the horizontal velocity but to the mass flux (cf. Eqs. 3 and 4). Since the mass flux is not a prognostic variable but needs to be derived, an accurate edge-mean is not available. In ICON and in many other models the interpolation of density (or equivalent variables) from neighboring cells to edges gives a second order mass flux on a regular grid. It can be shown analytically that if the edge-mean mass flux is approximated to *m*-th order, *m* being a positive even number, the divergence operator on an equilateral triangle will be of order $m-1$, and the sign of the leading error depends on the orientation of the triangle. (Detailed derivation can be found in Appendix B.4 of Wan (2009), available from http://www.mpimet.mpg.de/en/science/publications/reports-on-earth-system-science.html.)

In summary, the truncation error analysis shows that the divergence operator defined on the triangular C-grid yields a checkerboard error pattern. This appears to be an inherent property related to the cell shape and the placement of the velocity variables. The curl and gradient operators, on the other hand, are second-order accurate on the regular planar grid due to the symmetric geometry. The derivations are omitted in this paper.

4.3 Noise control

The checkerboard error pattern highlighted by the analysis in Sect. 4.2 enters the hydrostatic model system because of the continuity equation (3) and the temperature advection term in Eq. (2) (cf. the discrete form in Sect. 5.5). Grid scale noise in the divergence operator typically causes noise in the surface pressure p_s and temperature T, which then affects the velocity field through the pressure gradient force. Such numerical noise, while less apparent in the barotropic tests reported in BR05 and Rípodas et al. (2009), significantly affects three-dimensional baroclinic simulations. One possibility to avoid this problem is to improve the divergence operator by enlarging the stencil. For example, with a four-cell stencil (one triangle plus three of its direct neighbors, involving nine velocity points), one can construct a second-order divergence operator on a regular grid, and apply certain measures to approach second order in spherical geometry. Further discussions in this direction will be included in Part 2 of the paper. Here we only point out that, if the transport of tracers in the same model is to be handled by finite volume methods using a single cell as control volume, a different stencil for divergence in the dynamical core will destroy the tracer-and-air-mass consistency whose importance has been pointed out by, e.g. Lin and Rood (1996), Jöckel et al. (2001), Gross et al. (2002) and Zhang et al. (2008). In this paper, we rely instead on a carefully chosen numerical diffusion to suppress the checkerboard noise. Although it is generally not a preferred practice to use filtering or damping algorithms in numerical models, there is an interesting relationship between the discrete divergence and vector Laplacian on the triangular C-grid that can be exploited.

As in the ICON shallow water model described in Rípodas et al. (2009), the vector Laplacian

$$\nabla^2 \boldsymbol{v} = \nabla(\nabla \cdot \boldsymbol{v}) - \nabla \times (\nabla \times \boldsymbol{v}) \tag{13}$$

is approximated in an intuitive manner by

$$\left(\nabla_d^2 \boldsymbol{v}\right)_\mathrm{e} \cdot \boldsymbol{N}_\mathrm{e} = \mathrm{grad}_n\left[\mathrm{div}(\boldsymbol{v})\right] - \mathrm{grad}_\tau\left[\mathrm{curl}(\boldsymbol{v})\right]. \tag{14}$$

Here the subscript d denotes the discrete approximation, e the edge midpoint, and $\boldsymbol{N}_\mathrm{e}$ the unit normal vector associated to the edge. (The relationship between the unit normal vector $\boldsymbol{N}_\mathrm{e}$ of an edge and the outward unit vector $\boldsymbol{n}_\mathrm{e}$ of a cell that the edge belongs to is either $\boldsymbol{N}_\mathrm{e} = \boldsymbol{n}_\mathrm{e}$ or $\boldsymbol{N}_\mathrm{e} = -\boldsymbol{n}_\mathrm{e}$.) The notations div, curl, grad_n and grad_τ denote the discrete divergence, curl, normal gradient, and tangential gradient operators defined in Sect. 4.1. The divergence operator on a regular planar grid is defined by Eq. (6) in Sect. 4.2. The fourth-order hyper-Laplacian, widely used for horizontal diffusion in atmospheric models because of its scale selectivity, is approximated by

$$\nabla_d^4 \boldsymbol{v} = \nabla_d^2 \left(\nabla_d^2 \boldsymbol{v}\right). \tag{15}$$

Like in the previous subsection, one can perform a Taylor expansion (but with respect to the edge midpoint e) and get

$$\left(\nabla_d^4 \boldsymbol{v}\right)_\mathrm{e} \cdot \boldsymbol{N}_\mathrm{e} = \left(\nabla^4 \boldsymbol{v}\right)_\mathrm{e} \cdot \boldsymbol{N}_\mathrm{e} + (-1)^\delta 48\sqrt{3}\, l^{-2} H(\boldsymbol{v})_\mathrm{e} + \mathcal{O}(l^0). \tag{16}$$

The function H is the same as in Eq. (7).

Assuming that the dynamical core uses a diffusion coefficient $\mathcal{K}_4$ and time step Δt, if Eq. (16) is multiplied by $(-\Delta t\, \mathcal{K}_4)$, applying the divergence operator, and retaining only two leading terms on the right-hand side yields

$$\mathrm{div}\left(-\Delta t\, \mathcal{K}_4 \nabla_d^4 \boldsymbol{v}\right) = -\Delta t\, \mathcal{K}_4 24^2 l^{-3} (-1)^\delta H(\boldsymbol{v})_o - \Delta t\, \mathcal{K}_4\, \mathrm{div}\left(\nabla^4 \boldsymbol{v}\right)_o + \cdots \tag{17}$$

Now we apply Eq. (7) to the second term on the right-hand side of Eq. (17), use a symbol $\mathbb{E}_{\mathrm{div},1}$ to denote the first order term in Eq. (7), i.e.

$$\mathbb{E}_{\mathrm{div},1} = (-1)^\delta\, l\, H(\boldsymbol{v})_o\,, \tag{18}$$

and let $\hat{l} = l/\sqrt{3}$ to denote the distance between neighboring cell centers. After some manipulation, Eq. (17) becomes

$$\mathrm{div}\left(-\Delta t\, \mathcal{K}_4 \nabla_d^4 \boldsymbol{v}\right)_o = -\Delta t\, \mathcal{K}_4 \left(\sqrt{8}/\hat{l}\right)^4 \mathbb{E}_{\mathrm{div},1} - \Delta t\, \mathcal{K}_4 \left[\nabla^4 (\nabla \cdot \boldsymbol{v})\right]_o + \cdots \tag{19}$$

This shows that, when the vector Laplacian (Eq. 15) is used in the explicit numerical diffusion for horizontal wind, apart from the hyper diffusion one usually expects (i.e. the second term on the right-hand side of Eq. 19), there is an additional effect that compensates (at least to some extent) the leading error in divergence. This additional effect is similar to the divergence damping mechanism that has been adopted in many dynamical cores (e.g. Lin, 2004). Furthermore, if the coefficient $\mathcal{K}_4$ is determined via a parameter τ^* using the formula

$$\mathcal{K}_4 = \frac{1}{\tau^*}\left(\frac{\hat{l}}{\sqrt{8}}\right)^4, \tag{20}$$

then $\Delta t/\tau^*$ indicates the fraction of the checkerboard divergence error that can be removed after one time step.

In our numerical experiments it has been observed that the ratio $\Delta t/\tau^* = 1$ is very effective in removing the grid-scale noise and renders a reasonably stable model configuration. Furthermore, given that the icosahedral grid is not strictly regular in terms of cell sizes and edge lengths, we use the local edge length for Eq. (20) instead of the global mean, which further improves the effectiveness of the method. Examples in the shallow water model can be found in (Rípodas et al., 2009).

It should be mentioned, however, that this approach does have a clear disadvantage. The two terms on the right-hand side of Eq. (19) are controlled by the same $\mathcal{K}_4$ coefficient. Because the value of $\mathcal{K}_4$ has to be chosen to achieve a sufficient compensation of the checkerboard error, there is no longer the freedom to choose the magnitude of the hyper-diffusion by physical arguments only. Since the characteristic damping time τ^* corresponding to $\Delta t/\tau^* = 1$ is considerably shorter than usually seen in climate models, there is a danger of overly strong diffusivity in our triangular ICOHDC. This is in fact one of the major concerns we have regarding the viability of this dynamical core in long-term climate simulations, and a point to which special attention will be paid in the future.

Title Page
Abstract | Introduction
Conclusions | References
Tables | Figures
◀| |▶
◀ ▶
Back | Close
Full Screen / Esc
Printer-friendly Version
Interactive Discussion

5 Discrete formulation of the dynamical core

We introduce now the discrete form of the primitive Eqs. (1)–(4) employed in the ICOHDC.

5.1 Horizontal interpolation

On a staggered horizontal grid, the normal wind and the relative vorticity are not co-located with mass (and temperature). Horizontal interpolation is thus necessary. The following interpolations are used in the ICOHDC:

- $\overline{\psi}^{\mathrm{c2e}}$, linear interpolation of a scalar ψ from two neighboring cell centers to the midpoint of the shared edge;
- $\overline{\psi}^{v\mathrm{2e}}$, linear interpolation of a scalar ψ from two vertices of an edge to its midpoint (i.e. arithmetic average).
- $\overline{\psi}^{\mathrm{e2c,lin}}$, a bilinear interpolation from the three edges of a triangle to its circumcenter. The interpolation is performed in a local spherical coordinate whose equator and primal meridian intersect at the cell center.
- $\overline{\psi}^{\mathrm{e2c,aw}}$, an area-weighted interpolation

$$\overline{\psi}^{\mathrm{e2c,aw}} = \sum_{\mathrm{e}} \frac{A_{\mathrm{c,e}}}{A_{\mathrm{c}}} \psi_{\mathrm{e}} \tag{21}$$

where A_{c} is the cell area, and $A_{\mathrm{c,e}}$ the area of a sub-triangle defined by the cell center c and the two vertices of edge e (Fig. 5a).

5.2 Vorticity flux and kinetic energy gradient

The first two terms on the right-hand side of Eq. (1), i.e. the absolute vorticity flux and the kinetic energy gradient, represent the combination of horizontal momentum advection and Coriolis force in vector invariant form. The kinetic energy gradient is calculated in our model by

$$\mathrm{grad}_n\left(\overline{0.5\left(v_n^2+v_\tau^2\right)}^{\mathrm{e2c,lin}}\right), \tag{22}$$

and the absolute vorticity flux by

$$\left(f+\overline{\mathrm{curl}(\boldsymbol{v})}^{v2\mathrm{e}}\right)v_\tau\,. \tag{23}$$

As mentioned earlier, the C-grid discretization predicts only the normal component of the horizontal wind. The tangential wind v_τ needed by Eqs. (22) and (23) is reconstructed at edge midpoints using the vector radial basis functions (RBFs) introduced in Narcowich and Ward (1994), with an inverse multiquadric kernel. For a more complete description and testing of this algorithm we refer to Ruppert (2007) and Bonaventura et al. (2011). The stencil involves four edges surrounding the target one (Fig. 5b). Following BR05, it is assumed that the normal and tangential components form a right-hand system.

5.3 Pressure and layer thickness

The η coordinate of Simmons and Strüfing (1981), a terrain following coordinate near the Earth's surface that gradually transforms into pressure coordinate in the upper troposphere, has been widely used in atmospheric GCMs. Here we only mention a few technical details for completeness and clarity: the pressure at layer interfaces (see Fig. 1) is given by

$$p_{k+1/2}=A_{k+1/2}+B_{k+1/2}\,p_\mathrm{s}\,,\quad k=0,1,\ldots,NLEV\,. \tag{24}$$

Here p_s stands for surface pressure. $NLEV$ is the total number of vertical layers. A and B are predefined parameters (see, e.g. Roeckner et al., 2003). $B=\partial p/\partial p_\mathrm{s}$ is used in Eq. (4). The pressure thickness of the k-th model layer is denoted by Δp_k $\left(= p_{k+1/2} - p_{k-1/2}\right)$.

5.4 Continuity equation

To compute the right-hand side of Eq. (3) the divergence operator is applied to the mass flux $\boldsymbol{v}\,\partial p/\partial\eta$, followed by an integral through the vertical column. This discretization does not introduce any spurious sources or sinks in the total air mass, as long as the mass flux has a unique value at each edge. In this paper, the air mass flux in the normal direction $\boldsymbol{N}_\mathrm{e}$ of an edge e is computed by

$$v_n\overline{(\partial p/\partial\eta)}^{\mathrm{c2e}}\,. \tag{25}$$

5.5 Horizontal advection of temperature

The horizontal advection of temperature at cell c in layer k is discretized in an energy-conserving form

$$(\boldsymbol{v}\cdot\nabla T)_{\mathrm{c},k} = \frac{1}{\Delta p_{\mathrm{c},k}}\left[\mathrm{div}(\boldsymbol{v}\,\Delta p T)_{\mathrm{c},k} - T_{\mathrm{c},k}\mathrm{div}(\boldsymbol{v}\,\Delta p)_{\mathrm{c},k}\right]. \tag{26}$$

The mass flux divergence in this equation is the same as in the discrete continuity equation. The heat flux divergence is calculated by first interpolating temperature and layer thickness separately from cells to edges, multiplying by the normal wind and then applying the discrete divergence operator.

5.6 Vertical advection of momentum and temperature

The vertical advection terms in Eqs. (1) and (2) are discretized in the same way as in ECHAM following Simmons and Burridge (1981, hereafter SB81):

$$\left(\dot{\eta}\frac{\partial\psi}{\partial\eta}\right)_k = \left(\dot{\eta}\frac{\partial p}{\partial\eta}\frac{\partial\psi}{\partial p}\right)_k$$

5 $$= \frac{1}{2\Delta p_k}\left\{\left(\dot{\eta}\frac{\partial p}{\partial\eta}\right)_{k+1/2}(\psi_{k+1}-\psi_k) + \left(\dot{\eta}\frac{\partial p}{\partial\eta}\right)_{k-1/2}(\psi_k-\psi_{k-1})\right\}. \tag{27}$$

Here ψ is either temperature or a horizontal wind component. The vertical indices are illustrated in Fig. 1. The vertical velocities at layer interfaces are diagnosed by Eq. (4). Note that Eq. (27) can be derived by applying the idea of Eq. (26) to the vertical direction, then replacing the divergence operator by the central difference, and the cell-to-edge interpolation by the arithmetic average.

For the advection of the normal wind in the ICOHDC, Eq. (27) requires layer thickness and vertical velocity at edge midpoints. These are obtained by the linear interpolation mentioned earlier in Sect. 5.4.

5.7 Hydrostatic equation

The hydrostatic equation involves only vertical discretization, thus takes the same form in the ICOHDC as in SB81 and in the spectral core of ECHAM. The discrete counterpart of Eq. (5) reads

$$\Phi_{\mathrm{c},k+1/2} = \Phi_{\mathrm{c,s}} + \sum_{j=k+1}^{NLEV} R_d T_{\mathrm{c},j} \ln\left(\frac{p_{\mathrm{c},j+1/2}}{p_{\mathrm{c},j-1/2}}\right) \tag{28}$$

for layer interfaces with $k \geqslant 1$. Here $\phi_{c,s}$ denotes the surface geopotential at cell c. The geopotential at full levels are given by

$$\phi_{c,k} = \phi_{c,k+1/2} + \alpha_{c,k} R_d T_{c,k} \tag{29}$$

where

$$\alpha_{c,k} = \begin{cases} \ln 2\,, & \text{for } k = 1\,; \\ 1 - \frac{p_{c,k-1/2}}{\Delta p_{c,k}} \ln\left(\frac{p_{c,k+1/2}}{p_{c,k-1/2}}\right), & \text{for } k > 1\,. \end{cases} \tag{30}$$

5.8 Pressure gradient force and adiabatic heating

After computing the geopotential by Eq. (29), the last term in the velocity Eq. (1) can be obtained by applying the normal gradient operator.

The pressure gradient term in the same equation is calculated by

$$(R_d T \nabla \ln p)_e \cdot \boldsymbol{N}_e = R_d \overline{T}^{c2e} \mathrm{grad}_n \left[\frac{p_{k+1/2} \ln p_{k+1/2} - p_{k-1/2} \ln p_{k-1/2}}{\Delta p_k} \right]. \tag{31}$$

Using Eq. (31), the first part of the adiabatic heating term in the temperature equation (2) can be obtained by

$$\left(\frac{R_d T}{p} \boldsymbol{v} \cdot \nabla p \right)_{c,k} = \frac{\overline{2 v_n \Delta p \left[(R_d T \nabla \ln p) \cdot \boldsymbol{N}_e \right]}^{e2c,aw}}{\Delta p_{c,k}}. \tag{32}$$

The remaining part is approximated by

$$\left[\frac{R_d T}{p} \left(\frac{\partial p}{\partial t} + \dot{\eta} \frac{\partial p}{\partial \eta} \right) \right]_{c,k} = \\ - \frac{R_d T_{c,k}}{\Delta p_{c,k}} \left[\ln \left(\frac{p_{c,k+1/2}}{p_{c,k-1/2}} \right) \sum_{j=1}^{k-1} \mathrm{div}\,(\boldsymbol{v} \Delta p)_{c,j} + \alpha_{c,k} \, \mathrm{div}\,(\boldsymbol{v} \Delta p)_{c,k} \right]. \tag{33}$$

Both Eqs. (32) and (33) are derived following the energy conservation constraint in SB81.

5.9 A few remarks on the spatial discretization

In this section we have mentioned repeatedly the C-grid discretization of SB81, which is an energy-conserving scheme on regular latitude-longitude grids, designed for an early finite-difference version of the NWP model of the European Centre for Medium-range Weather Forecasts. In the baseline version of the ICOHDC, the kinetic energy gradient and the absolute vorticity flux discretized on the triangular grid (Eqs. 22 and 23) do not guarantee energy conservation to machine precision, partly due to the tangential wind reconstruction using the RBFs. The other discrete formulae described in Sects. 5.4–5.8, on the other hand, do help avoid spurious energy sources/sinks.

Potentially, there might be another issue related to the RBF reconstruction. As discussed in Hollingsworth et al. (1983) and Gassmann (2012), certain inconsistencies between the discrete vorticity flux and kinetic energy gradient can trigger nonlinear instability that manifests itself as small scale noise at high resolutions. So far we have not seen clear evidences of such instability in the test results of the ICOHDC (cf. Sect. 6).

5.10 Time stepping scheme

In the baseline version of the ICOHDC we use a time stepping method similar to that of the ECHAM dynamical core. This consists of the leapfrog scheme, the Asselin (1972) filter, and the widely used semi-implicit correction scheme for linear gravity waves (see, e.g. SB81). The reference atmosphere used by the semi-implicit correction is isothermal ($T^r = 300\,\mathrm{K}$), at rest ($\boldsymbol{v}^r = 0$) on a flat surface ($\phi_s^r = 0$) with constant surface pressure ($p_s^r = 800\,\mathrm{hPa}$). To achieve computational efficiency, the resulting 3-D Helmholtz equation of divergence is decomposed into a series of 2-D equations, each corresponding to one vertical mode. The 2-D equations associated with phase speed higher than 30 m s^{-1} are numerically solved using the generalized minimal residual method (GMRES, Saad and Schultz, 1986).

In the standard model configuration the time stepping scheme uses the following parameters. The Asselin coefficient is 0.1 following ECHAM. In the semi-implicit correction, coefficients of the gravity wave terms evaluated at the old and new time steps are set to 0.3 and 0.7, respectively, following the global forecast model GME of the German Weather Service (Majewski et al., 2002). Detailed formulation of the time integration algorithm is given in Appendix B.

6 Idealized dry dynamical core tests

In this section we present some results of numerical simulations carried out to evaluate the new dynamical core. The goal here is to find out whether the present version of the ICOHDC can correctly represent basic processes of the adiabatic atmospheric dynamics, and to analyze the sensitivity of the numerical solutions to horizontal resolution. During the development of the new dynamical core we routinely perform a suite of idealized dry dynamical core tests with different levels of complexity. The simplest ones are 3-D extensions of the widely used shallow water tests 5 and 6 from Williamson et al. (1992). The barotropic cases are in some sense a sanity check for the 3-D formulation of the ICOHDC and its practical implementation in the code. These results can be found in Wan (2009), and are not repeated here. In this section, we concentrate our discussions on two deterministic baroclinic tests (Sect. 6.1) and an idealized dry "climate" test (Sect. 6.2).

All results presented in this section are obtained using revision 6489 of the ICON code. The vertical grid is fixed at L31, which resolves the atmosphere from the surface to 10 hPa. This grid has been commonly used in ECHAM (see, e.g. Roeckner et al., 2006). The triangular grids of the new dynamical core are optimized using the algorithm of Tomita et al. (2001) with the spring coefficient being 0.90.

6.1 Deterministic baroclinic tests

The test case proposed by Jablonowski and Williamson (2006a,b, hereafter JW06) has been widely used in recent years for testing 3-D atmospheric dynamical cores. Inspired by the baroclinic instability theory, the deterministic test consists of two parts: a steady state test followed by a baroclinic instability test.

6.1.1 Steady state test

In the first part of the test, the dynamical core is initialized with a zonally symmetric, geostrophically balanced condition specified by analytical functions. Since this initial condition is a steady state solution of the primitive equations, a perfect numerical model would retain the initial state to machine precision. The spectral core of ECHAM can preserve the zonal symmetry in an arbitrarily long integration. Meanwhile, the model state evolves continuously (but very slowly) from the initial state because of the horizontal diffusion. In the ICOHDC, zonal asymmetries are triggered immediately after model initialization due to grid irregularity near the pentagon points (cf. Sect. 3), resulting in wavenumber 5 patterns near 26.6° N/S. Embedded in the dynamically unstable mean state of this test case, the perturbations amplify for more than 10 days, then reach a quasi-equilibrium state after 20 to 30 days (not shown). As the horizontal resolution increases, the magnitude of the numerical errors is reduced and the perturbations evolve less rapidly. These behaviors agree with our expectation, and are similar to the results of the GME model (also built on icosahedral grids) presented in JW06.

6.1.2 Baroclinic wave test and equivalent resolutions

The second part of this test case focuses on the evolution of an idealized baroclinic wave in the Northern Hemisphere, triggered by an analytically specified large-scale perturbation in the wind field. Cyclone-like structures develop in the course of about 10 days, featuring lows and highs in the surface pressure field (Fig. 6, left column) and accompanying fronts in the lower troposphere temperature (Fig. 6, right column). This figure shows the ICOHDC simulation at R2B5 resolution which has an average grid spacing of 70 km between neighboring mass points. The key features of the simulated baroclinic wave evolution, including the slow development of the perturbations in the first 6 days and the subsequent exponential intensification, as well as the magnitude of the closed cells in surface pressure and the fronts in temperature, agree well with the reference solutions given by JW06.

Figure 7 shows the same fields but after 9 days of integration, and at 5 different horizontal resolutions. The average grid spacing between mass points ranges from 280 km (at R2B3) to 17.5 km (at R2B7). The solution obtained on the coarsest grid (R2B3) is of unsatisfactory quality, in that the depressions are too weak, while the spurious perturbations at the rear of the wave train are too strong. This resolution is thus not recommended for future applications of the new dynamical core. The next solution, at R2B4, is significantly improved, although the first two low pressure cells are still somewhat weak, and there is an easily detectable phase lag in the propagation of the wave in comparison with the solution at R2B7. As the grid is further refined, the phase lag gets smaller, and the depressions become deeper. The two runs at the highest resolutions look very similar, and are hardly distinguishable from the reference solutions in JW06 by visual comparison.

To quantitatively assess the convergence of these numerical solutions, we follow JW06 and use the l_1, l_2 and l_∞ differences norms of surface pressure as the metric. In the work of JW06 it was found that differences among solutions from four models using very different discretization methods stopped decreasing once the resolutions increased beyond a certain limit. Based on this observation, the uncertainty in their reference solutions was estimated. The corresponding uncertainties in the difference norms are shown by the yellow shading in Fig. 8. When the difference norms fall below the uncertainty limit, the solution being tested is considered as of the same quality as the reference solution.

In Fig. 8 the norms of p_s differences are shown between the R2B3 to R2B6 simulations and the R2B7 run (upper row), as well as between the ICOHDC simulations and a reference solution in JW06 from the National Center for Atmospheric Research Semi-Lagrangian dynamical core (NCAR SLD, Fig. 8 second row). Difference norms computed against the other reference solutions in JW06 are very similar (not shown). Regardless of the choice of reference, panels in Fig. 8 clearly indicate a decrease in the difference norms when the horizontal resolution increases. Convergence of the numerical solution is achieved at R2B6. The R2B6 and R2B7 solutions are able to represent the baroclinic wave evolution within the uncertainty in the reference solution.

Since the ultimate purpose of developing the new dynamical core is to use it in climate research, a natural question one would expect from the potential users, especially from those having been using ECHAM, is the equivalent resolutions between the ICOHDC and the spectral core. In Fig. 9 the ICOHDC results are presented side-by-side with simulations from the spectral core at four spectral resolutions that have been used for the full model in various applications. By comparing the strength of the vortices, the magnitude of the horizontal gradients, and the level of details of the characteristic patterns represented by the models, we come to the conclusion that each ICOHDC solution in this figure is of slightly higher resolution than the spectral model results shown in the same row. The difference of the spectral model results w.r.t. the NCAR SLD solution is shown in Fig. 10. Note that although from the 850 hPa vorticity snapshots in Fig. 9 we conclude that R2B5 is higher than T85, the T85 simulation captures the reference solution within the uncertainty while R2B5 does not. According to the snapshots, the errors in the lower resolution spectral model results are mainly in the strength of the vortices and the spatial gradients, while in the ICOHDC the phase speed is also a major source of numerical error.

Phase error is a typical problem associated with dynamical cores using second (or lower) order spatial discretization methods. It is also one of the main disadvantages of such models at medium and low resolutions in comparison with the spectral transform method. It is worth noting that in JW06 the finite-difference model GME has a similar phase problem, while the NCAR finite volume core (Lin, 2004), which uses the third-order piecewise parabolic advection algorithm, does not. Skamarock and Gassmann (2011) showed that in the ICON non-hydrostatic model (Gassmann, 2010) and in the Model for Prediction Across Scales (MPAS; Skamarock et al., 2010), replacing the second-order potential temperature transport by third-order schemes can significantly reduce the magnitude of the phase error in this test case and suppress its growth. For the hydrostatic dynamical core discussed here, it will probably also be beneficial to use a higher-order scheme for temperature advection in Eq. (26) in Sect. 5. On the other hand, Fig. 9 also suggests that the phase error in the ICOHDC becomes negligible at R2B6 (35 km). Since the ICON models are developed for high-resolution modelling, the phase error is not expected to be an obstacle in real applications of the new model system.

Coming back to the question of equivalent resolutions, we have performed the baroclinic wave test at several other resolutions in addition to those in Fig. 9, both with the ICOHDC and with the spectral core of ECHAM, and established the relationships presented in Table 2. The equivalent resolutions (in this particular test case) are established by the following procedure: first, simulations are performed on all the icosahedral grids listed in the table, and at the spectral truncations given without parenthesis (see Table 2). From visual comparisons similar to Fig. 9, we establish resolution pairs like R5B3–T63, R2B5–T106, etc., that produce similar results. It turns out that for these visually identified pairs, the ratios between the average grid spacing of different icosahedral grids match well with the ratios between the corresponding truncation wavenumbers. Using this relationship, we then derived the wavenumbers given in parenthesis, which are not “standard” resolutions of the ECHAM model. In principle, it would be useful to verify the established equivalent resolutions in some quantitative manner, for example by calculating the difference norms of surface pressure in each pair, and comparing them with the uncertainty estimates (the yellow shading in Figs. 8 and 10). At the current stage, however, the difference norms between the medium- and low-resolution pairs would lie outside the uncertainty range unless the phase error in the ICOHDC was reduced. The verification is thus not done in this study.

It is interesting to notice that, in the table, the average grid spacings of the ICON grids match well the zonal grid size at 60° N on the Gaussian grids of the corresponding spectral resolution. This is probably not a coincidence, but a result of the fact that in this test case the baroclinic wave evolves and propagates near this latitude. Nonlinear terms in the primitive equations play a crucial role in the baroclinic instability development. In both models these terms are computed in grid-point space, and using similar discretization schemes following the work of SB81. It is thus not surprising that the equivalent resolutions we identified turn out to have similar spacing at 60° N. In a different test case that features dynamical processes confined to, say, the tropics, the conclusions on equivalent resolutions will probably be different.

From the perspective of the numerical solution of partial differential equations, one may attempt to establish equivalent resolutions by comparing the total number of degrees of freedom (DOF). The DOF alone, however, is not a very relevant index if the two models in question use vastly different numerics. The order of accuracy of the numerical schemes, the algorithmic complexity, and the amount of arithmetic computations involved in solving a single degree of freedom need to be taken into account as well. In our case, the ICOHDC uses rather simple finite-difference schemes of relatively low (first and second) order, while the spectral core requires Fourier and Legendre transform in each integration step, and is accurate to infinite order in problems where the simulated flow is smooth. It thus should not be expected that equivalent resolutions between the two cores have the same total DOF. For the hydrostatic model, if we define the DOF of one vertical level to be the total number of prognostic equations, i.e. velocity plus temperature grid points for the ICOHDC, and in the case of the spectral model the total number of spectral coefficients of vorticity, divergence and temperature of the resolved wavenumbers,[1] then the ratio of DOF between the equivalent resolutions we

---

[1] The continuity equation is ignored here because hydrostatic models uses surface pressure as the prognostic variable which is defined only at the Earth's surface.

identified above is about 6–7 to 1 (ICOHDC to spectral). To put the number into perspective, one can do a similar computation for the resolutions presented in JW06 for the GME model and the NCAR Finite Volume (FV) and spectral cores, to get the ratios 5.5 : 1 (GME versus spectral) and 7 : 1 (FV versus spectral), respectively.

As a note of caution, we emphasize again that the equivalent resolutions presented in Table 2 are established for this particular case. For other dynamical core tests and for the idealized and real-world simulations performed with parameterizations, these relations do not necessarily hold.

In the simulations presented in Fig. 7 and Table 2, the ICOHDC time step is 1200 s at R2B3, and decreases linearly with the average grid spacing (Table 2). The simulated flow does not appear noisy (cf. e.g. Fig. 9). These indicate that the grid-scale noise originating from the divergence operator is effectively suppressed by the kind of horizontal diffusion employed. Meanwhile, the simulated baroclinic vorticies are strong at high resolutions and the horizontal gradients sharp (Fig. 9). In this comparison, there is no clear evidence of overly strong damping in the ICOHDC.

6.2 Held-Suarez test

After the adiabatic deterministic test cases discussed above, we consider here the dry “climate” experiment proposed by Held and Suarez (1994), in which the dynamical core is forced by Rayleigh damping of horizontal wind in the near-surface layers as well as relaxation of the temperature field towards a prescribed, north-south and zonally symmetric radiative equilibrium. The original goal of this popular test was to evaluate the zonal-mean climatology obtained from the last 1000 days of a 1200-day simulation. However, a more comprehensive analysis of the inherent low-frequency variability was carried out in Wan et al. (2008), where an ensemble approach was proposed for the evaluation of the results. Here we follow this approach and perform ensembles consisting of 10 independent 300-day integrations. Each integration starts from the JW06 zonally symmetric initial condition with random noise of magnitude $1\,\mathrm{m\,s^{-1}}$ added to the wind field. (This choice is rather arbitrary. As long as the 10 integrations within an ensemble are independent, the conclusions drawn in this subsection are not affected by the initial condition.) Simulations are performed at resolutions R2B3, R2B4 and R2B5 using the same configurations as in the deterministic test cases. The zonal-mean climate states are diagnosed from the last 100 days of each integration.

Figure 11 presents the ensemble mean model climate at R2B5. Although simple by design, the Held-Suarez test is able to reproduce many realistic features of the global circulation. Baroclinic eddies cause strong poleward heat and momentum transport (Fig. 11d and c, respectively). The heat transport reduces the meridional temperature gradient in comparison to the prescribed radiative equilibrium (Fig. 11b, here in comparison to Fig. 1c in Held and Suarez, 1994). The meridional transport of angular momentum converges in the mid-latitudes, forming a single westerly jet in each hemisphere (Fig. 11a). The core regions of the jets are located near 250 hPa. The maximum time- and zonal-mean zonal wind is about 30 $\mathrm{m\,s^{-1}}$. Easterlies appear in the equatorial and polar lower atmosphere, as well as in the tropics near the model top. The baroclinic wave activities concentrate in the mid-latitudes, as depicted by the transient eddy kinetic energy and temperature variance (Fig. 11e and f). The single maximum of eddy kinetic energy in each hemisphere appears in the upper troposphere near 45° latitude, close to the core region of the westerly jet. Easterlies in the tropics show little variance. In each hemisphere, the maximum temperature variance appears near the Earth's surface and extends upward and poleward. A second maximum of smaller magnitude occurs near the tropopause. These features of the simulated circulation agree well with results reported in the literature (e.g. Held and Suarez, 1994; Jablonowski, 1998; Lin, 2004; Wan et al., 2008).

Sensitivity of the ICOHDC results to horizontal resolution is revealed by Figs. 12 and 13. The contour lines show the differences in the ensemble average of the quantities displayed in Fig. 11, while the gray and light-blue shadings indicate where the differences are significant (at 0.05 and 0.01 significance levels, respectively) according to the Kolmogorov-Smirnov test (Press et al., 1992). Comparing R2B3 with R2B5, the increase in horizontal resolution leads to a substantial enhancement of the eddy activity in the mid-latitudes, stronger poleward transport, and consequently higher temperature in the Polar Regions as well as a poleward shift of the westerly jets. The differences between the R2B4 and R2B5 ensembles are much smaller (Figs. 13). Although one can still see enhancement in the eddy activities in Fig. 13d–f and temperature differences in high altitudes/latitudes regions in Fig. 13b, the discrepancies are generally much less significant than between R2B3 and R2B5. Figures 12 and 13 together show a clear trend of convergence in the ICOHDC results.

7 First results from the aqua-planet experiments

In the previous section we have evaluated the ICOHDC using dry dynamical core tests at various resolutions. On the whole, the new core produces results that agree reasonably well with those from the spectral core of ECHAM, as well as with the reference solutions available in the literature. It turns out that in these test cases, the grid-scale noise discussed in Sect. 4 is well under control and has not yet brought obvious detrimental effects. One might argue that when moist processes are included in the model, condensational heating will act as a positive feedback which will amplify the grid-scale noise and make the model unstable. To find out whether this is the case, we perform aqua-planet simulations following the proposal of Neale and Hoskins (2000). The simulations are carried out using revision 6489 of the ICON code.

For this exercise, the ICOHDC is coupled to the cumulus convection, large-scale condensation, turbulent mixing and radiation parameterizations of the ECHAM6 model (Giorgetta et al., 2012). Second-order horizontal diffusion is applied to the three uppermost model layers to enhance horizontal damping. This is a widely used technique in climate models to effectively dissipate upward propagating waves of various scales and avoid spurious reflection of the vertically propagating waves triggered by cumulus convection and other sub-grid processes. Radiative transfer calculation is performed every other hour as in ECHAM. We refer to the resulting model configuration as the ICOsahedral Hydrostatic Atmospheric Model (ICOHAM).

Simulations are performed at R2B4L31 ($\Delta t = 480\,\mathrm{s}$) using the "Control" and "Qobs" sea surface temperature (SST) profiles of Neale and Hoskins (2000). The reference solutions are from ECHAM6 at T63L47 ($\Delta t = 600\,\mathrm{s}$). Both models are integrated for 1200 days. The last 800 days are used in the analysis presented in this paper. Here we do not attempt to investigate the convergence of the aqua-planet experiments (APE) from either ICOHAM or ECHAM6, because both models are new, and neither has been tuned at many resolutions. The intention here is rather to have a first look at the main features of the model climate. A more comprehensive evaluation of the ICOHAM aqua-planet simulations will be presented in a separate paper.

By comparing ICOHAM at R2B4 and ECHAM6 at T63 we are not suggesting that they are an equivalent pair. These resolutions are chosen because T63L47 is the most commonly used configuration of ECHAM6 (which has also been used in the CMIP5 simulations), while R2B4L31 is the resolution used by the ICOHDC and ICOHAM developers in the day-to-day routine tests. The L31 and L47 grids are identical between the surface and 100 hPa and thus differ only in the vertical extent and resolution above the tropopause.

The latitudinal variations of the simulated time- and zonal-mean surface precipitation rate in ICOHAM are shown in Fig. 14. In the "Control" case the total precipitation rate peaks at the equator and at about 35° latitudes, with the main contributors being cumulus convection and large-scale condensation, respectively. In the "Qobs" case, which has the same SST at the equator but weaker meridional gradients in the low latitudes, the tropical precipitation features two peaks, while the mid-latitude rainfall shifts slightly poleward. These results are reasonable in comparison to the APE Atlas (Williamson et al., 2011).

Next, we follow Williamson (2008) and consider the equatorial wave propagation characteristics. Figure 15 presents the wavenumber-frequency diagrams of tropical precipitation (meridionally averaged between 10° S–10° N), diagnosed using the methodology of Wheeler and Kiladis (1999). The quantity shown is the logarithm of the power of the symmetric component of the unnormalized spectra. It has been shown by

Williamson (2008) that the power of the background spectrum, usually used for normalizing the “raw” spectrum to identify spectral peaks, is sensitive to model resolution. In order not to lose such signal, we choose to show the raw spectra in Fig. 15, which are also meant to serve as a reference for future work. The normalized spectra are shown in Appendix C. The black lines that indicate the dispersion relationships of equatorial Rossby waves, Kelvin waves and inertia-gravity waves are the same as in Fig. 6 of Williamson (2008).

In both “Control” and “Qobs” simulations, the tropical precipitation has higher power at lower frequencies. The Kelvin waves are more evident in the “Control” case (upper row in Fig. 15), while the Rossby waves show the opposite sensitivity. Interestingly, the Rossby waves in ICOHAM show a clear peak at westward zonal wavenumber 5 in Fig. 15c. A question naturally arises whether this is an imprint of the icosahedral grid. It should be noted not only that the corresponding ECHAM simulation indicates a similar (albeit weaker) peak (Fig. 15d), but also that the APE Atlas has revealed wavenumber 5 features in the global circulation in many models that employ different types of grids and discretization methods (Williamson et al., 2011, Fig. 4.99). So far it is not yet clear whether and to what extent the icosahedral grid imprint is interacting with this mode.

Comparing the four panels in Fig. 15, one can see that on the whole, the power of the waves in ICOHAM at R2B4 is comparable to that in ECHAM6 at T63L47. The differences between the ICOHAM and ECHAM6 results are much smaller than the sensitivity to SST. This is an indication that the ICOHAM model behaves well in these simulations. In the future it will be useful to perform and analyze simulations at higher resolutions and assess the convergence of the model behavior.

8 Conclusions

In this paper we presented and evaluated a hydrostatic atmospheric dynamical core employing spherical triangular grids. The finite-difference discretization is based on the numerical techniques employed in the ICON shallow water model of Bonaventura

Title Page
Abstract Introduction
Conclusions References
Tables Figures
◂◂ ▸▸
◂ ▸
Back Close
Full Screen / Esc
Printer-friendly Version
Interactive Discussion

and Ringler (2005) and Rípodas et al. (2009), as well as the vertical discretization of Simmons and Burridge (1981). The baseline version of the new dynamical core ICOHDC uses leapfrog time stepping scheme, with additional semi-implicit correction to handle the fastest gravity waves.

The first outcome of this effort is improved understanding of the numerical properties of the C-grid discretization on triangular grids. Through the truncation error analysis, it is shown that the discrete divergence operator defined using the Gauss theorem is of first-order accuracy even on equilateral triangles. The leading error changes its sign from one cell to its immediate neighbors. This explains the grid-scale noise encountered in the development of the new dynamical core, and meanwhile provides useful hints for finding a remedy to control such noise through numerical diffusion. In recent years, similar problems on triangular C-grids have been reported and investigated by other modelling groups (e.g. Le Roux et al., 2007; Danilov, 2010). Our truncation error analysis provides more insight into the origin of the numerical noise from a different perspective.

After the theoretical analysis, the ICOHDC is evaluated using idealized test cases of various complexity. In this paper we have focused on the deterministic baroclinic instability test of Jablonowski and Williamson (2006a,b), carried out simulations at various horizontal resolutions, and compared the ICOHDC results with those from the spectral dynamical core of ECHAM and one reference model from NCAR. Longer, idealized "climate-like" simulations are also performed following the proposals of Held and Suarez (1994) and Neale and Hoskins (2000). On the whole the new dynamical core behaves well in the evaluation. In the dry dynamical core tests, the ICOHDC can correctly capture the key features of the dynamical processes in question. As the horizontal resolution increases, the numerical solutions clearly converge towards the references. In the aqua-planet experiments, the ICOHAM model is able to reproduce the same equatorial wave propagation characteristics as in ECHAM6, including the sensitivity of such characteristics to the meridional SST profile. At least in the dry tests down to 17 km grid spacing, and in the aqua-planet experiments at 140 km resolution,

Title Page
Abstract Introduction
Conclusions References
Tables Figures
◀| |▶
◀ ▶
Back Close
Full Screen / Esc

Printer-friendly Version

Interactive Discussion

the new model has not shown clear evidence of contamination by grid-scale noise or overly strong numerical damping. We thus conclude that the ICOHDC can serve as a good basis for further development of a global model for climate research.

In the next steps it will be useful to carry out more comprehensive analysis of the aqua-planet results, perform simulations at higher resolutions to investigate the interaction between numerical errors in the dynamical core and the parameterized moist physics, and investigate the impact of horizontal diffusion on long-term, aqua-planet and real-world climate simulations. In the ECHAM model, it has been observed that the precipitation and cloud fields simulated over the oceans typically feature wave-like patterns resulting from the Gibbs phenomenon associated with the spectral dynamical core. Such spurious responses to discontinuous forcing are not expected in the ICON models. It will be interesting to see what impacts this will have on climate simulations. Furthermore, the finite-difference methods and relatively small stencils used in the discretization of the ICOHDC make it less difficult to parallelize than the spectral core in high-resolution simulations using distributed memory. As the present paper focuses only on the accuracy of the numerical solutions, the computational efficiency and scalability of the new model will be reported elsewhere.

Appendix A

Cell-averaged divergence of the vector field defined by Eq. (11)

Assume a planar grid consisting of equilateral triangles with edge length l. Denote the center and the vertices of a generic cell by o and κ_j ($j = 1, 2, 3$, see Fig. 3), the Cartesian coordinates of which are (x_o, y_o) and (x_j, y_j), respectively. For the vector field defined by Eq. (10), the divergence averaged over the cell reads

GMDD
6, 59–119, 2013

A dynamical core on triangular grids – Part 1

H. Wan et al.

$$\left(\frac{\sqrt{3}\,l^2}{4}\right)^{-1}\iint\limits_{\text{cell}}\left(\frac{\partial u}{\partial x}+\frac{\partial v}{\partial y}\right)\mathrm{d}x\,\mathrm{d}y=\frac{\sqrt{70}\,D_x}{23\sqrt{\pi}\,l^2}\sin 2x_o+\frac{\sqrt{5}\,D_y}{11\sqrt{2\pi}\,l^2}\,, \tag{A1}$$

where

$$\begin{aligned}D_x = {} & 10\sqrt{3}(\sin y_3-\cos l\,\sin y_2)-(-1)^{\delta}\,24\sin l\,\cos y_2\\ & +2\sqrt{3}(\sin^3 y_3-\cos l\,\sin^3 y_2)+(-1)^{\delta}\,9\sin l\,\cos^3 y_2\end{aligned} \tag{A2}$$

$$\begin{aligned}D_y = {} & 2\sqrt{3}\,(2\cos 2y_3\cos x_3-\cos 2y_2\cos x_2-\cos 2y_1\cos x_1)\\ & +(-1)^{\delta}\,12\,(\sin 2y_2\sin x_2-\sin 2y_1\sin x_1)\,.\end{aligned} \tag{A3}$$

Appendix B

Leapfrog time stepping scheme with semi-implicit correction

For a generic prognostic equation

$$\frac{\partial\psi}{\partial t}=F(\psi) \tag{B1}$$

we denote the numerical solution given by the leapfrog scheme as

$$\psi^{n+1}_{\text{expl}}=\psi^{n-1}+2\,\Delta t\,F(\psi^n)\,. \tag{B2}$$

Here the superscripts denote time steps that are evenly distributed with interval Δt. Assume the forcing term on the right-hand side of Eq. (B1) can be split into a fast linear part F_{fl} and the slow and/or nonlinear part F_{sn}. The semi-implicit scheme can be formally written as

$$\left(\frac{\partial\psi}{\partial t}\right)^{n}=\frac{1}{2}\left[\theta F^{n+1}_{\text{fl}}+(2-\theta)F^{n-1}_{\text{fl}}\right]+F^{n}_{\text{sn}}\,, \tag{B3}$$

where $\theta/2$ is the weight of the implicitly evaluated forcing. Further manipulation of Eq. (B3) gives

$$\begin{aligned}\left(\frac{\partial\psi}{\partial t}\right)^n &= \underbrace{\frac{1}{2}\left[\theta F_{\mathrm{fl}}^{n+1} + (2-\theta)F_{\mathrm{fl}}^{n-1} - 2F_{fl}^{n}\right]} + \underbrace{\left(F_{\mathrm{fl}}^{n} + F_{\mathrm{sn}}^{n}\right)} \\ &= \qquad\quad \frac{1}{2}\Delta_{tt}^{\theta}F_{\mathrm{fl}} \qquad\qquad\quad + \qquad F^{n}\,.\end{aligned} \tag{B4}$$

Applying central difference to the left-hand side of Eq. (B4) and using Eq. (B2), one can get

$$\psi^{n+1} = \psi_{\mathrm{expl}}^{n+1} + \Delta t\,\Delta_{tt}^{\theta}F_{\mathrm{fl}}\,. \tag{B5}$$

In the following we use underlines to denote column vectors (matrices) containing discrete values of a quantity defined at all vertical layers at the same horizontal location, e.g.

$$\underline{\boldsymbol{v_n}} = \left(v_{n_1}, v_{n_2}, \ldots, v_{n_{\mathrm{NLEV}}}\right)^T\,, \tag{B6}$$

$$\underline{\boldsymbol{T}} = \left(T_1, T_2, \ldots, T_{\mathrm{NLEV}}\right)^T\,, \tag{B7}$$

$$\underline{\boldsymbol{D}} = \left(D_1, D_2, \ldots, D_{\mathrm{NLEV}}\right)^T\,, \tag{B8}$$

in which D stands for divergence, and the superscript T denotes matrix transpose. Using the reference atmosphere defined in Sect. 5.10 to linearize the following gravity wave related terms

$$F\left(\boldsymbol{v}\right)_{\mathrm{fl}} = -\frac{R_d T}{p}\nabla p - \nabla\phi\,, \tag{B9}$$

$$F\left(T\right)_{\mathrm{fl}} = \frac{R_d}{C_p}\frac{T}{p}\frac{dp}{\mathrm{d}t}\,, \tag{B10}$$

$$F\left(p_{\mathrm{s}}\right)_{\mathrm{fl}} = -\int_0^1 \nabla\cdot\left(\boldsymbol{v}\frac{\partial p}{\partial\eta}\right)\mathrm{d}\eta\,, \tag{B11}$$

one can derive the semi-implicit leap-frog scheme for normal velocity, temperature and surface pressure in the following form:

$$\underline{\boldsymbol{v}_{\boldsymbol{n}}}^{n+1} = \left(\underline{\boldsymbol{v}_{\boldsymbol{n}}}\right)^{n+1}_{\mathrm{expl}} - \Delta t\,\nabla\left(\underset{\sim}{\boldsymbol{\gamma}}\,\Delta^{\theta}_{tt}\underline{\boldsymbol{T}} + \underline{\boldsymbol{h}}\,\Delta^{\theta}_{tt}p_{\mathrm{s}}\right)\,, \tag{B12}$$

$$\underline{\boldsymbol{T}}^{n+1} = \left(\underline{\boldsymbol{T}}\right)^{n+1}_{\mathrm{expl}} - \Delta t\,\underset{\sim}{\boldsymbol{\tau}}\,\Delta^{\theta}_{tt}\underline{\boldsymbol{D}}\,, \tag{B13}$$

$$p_{\mathrm{s}}^{n+1} = \left(p_{\mathrm{s}}\right)^{n+1}_{\mathrm{expl}} - \Delta t\,\underline{\boldsymbol{\nu}}^{T}\,\Delta^{\theta}_{tt}\underline{\boldsymbol{D}}\,. \tag{B14}$$

The square matrices $\underset{\sim}{\boldsymbol{\gamma}}$, $\underset{\sim}{\boldsymbol{\tau}}$ and column vectors $\underline{\boldsymbol{h}}$, $\underline{\boldsymbol{\nu}}$ are defined as

$$\left(\underset{\sim}{\boldsymbol{\gamma}}\right)_{kj} = \begin{cases} 0 & \text{for } j < k \\ R_d\,\alpha^r_k & \text{for } j = k \\ R_d \ln\left(\dfrac{p^r_{j+1/2}}{p^r_{j-1/2}}\right) & \text{for } j > k \end{cases} \tag{B15}$$

$$\left(\underset{\sim}{\boldsymbol{\tau}}\right)_{kj} = \frac{\Delta p_j^r}{\Delta p_k^r}\,\frac{T^r}{C_p}\left(\underset{\sim}{\boldsymbol{\gamma}}\right)_{jk} \tag{B16}$$

$$\underline{\boldsymbol{\nu}} = \left(\Delta p_1^r, \Delta p_2^r, \cdots, \Delta p_{NLEV}^r\right)^T \tag{B17}$$

$$\underline{\boldsymbol{h}} = \frac{R_d T^r}{p_s^r}\,(1, 1, \cdots, 1)^T_{1\times NLEV}\ . \tag{B18}$$

Equations (B15–B18) can be seen a simplified version of the formulae in the appendix of Simmons and Burridge (1981). In the ICOHDC we have followed ECHAM and chosen an isothermal reference state, whilst the reference temperature in Simmons and Burridge (1981) changes with vertical level.

Define a time-independent matrix

$$\underset{\sim}{\mathbf{B}} = \underset{\sim}{\boldsymbol{\gamma}}\,\underset{\sim}{\boldsymbol{\tau}} + \underline{\boldsymbol{h}}\,\underline{\boldsymbol{\nu}}^T \tag{B19}$$

and the notation

$$\Delta^{\theta}_{tt,\mathrm{expl}}\,\psi = \theta\,\psi^{n+1}_{\mathrm{expl}} + (2-\theta)\,\psi^{n-1} - 2\psi^{n}\,. \tag{B20}$$

Use $\underset{\sim}{\mathbf{I}}$ to denote the $NLEV \times NLEV$ identity matrix. From Eqs. (B12)–(B14) the discretized Helmholtz equation of divergence can be obtained, which takes the form

$$\left[\underset{\sim}{\mathbf{I}} - (\theta\,\Delta t)^2\,\nabla_d^2\,\underset{\sim}{\mathbf{B}}\right]\Delta^{\theta}_{tt}\underline{\boldsymbol{D}} = \Delta^{\theta}_{tt,\mathrm{expl}}\,\underline{\boldsymbol{D}} - \theta\,\Delta t\,\nabla_d^2\left(\underset{\sim}{\boldsymbol{\gamma}}\,\Delta^{\theta}_{tt,\mathrm{expl}}\,\underline{\boldsymbol{T}} + \underline{\boldsymbol{h}}\,\Delta^{\theta}_{tt,\mathrm{expl}}\,p_s\right)\,. \tag{B21}$$

The discrete scalar Laplacian is defined as

$$\left(\nabla_d^2\,\psi\right) = \mathrm{div}\left[\mathrm{grad}_n(\psi)\right]\,. \tag{B22}$$

where div and grad_n are the discrete divergence and normal gradient operators, respectively.

The semi-implicit time integration scheme applied in the hydrostatic model can be summarized as the following algorithm:

1. Apply the explicit leapfrog scheme to obtain $\left(\underline{\boldsymbol{v}_n}\right)^{n+1}_{\text{expl}}$, $\underline{\boldsymbol{T}}^{n+1}_{\text{expl}}$ and $(p_\text{s})^{n+1}_{\text{expl}}$. Calculate $\Delta^{\theta}_{tt,\text{expl}}\underline{\boldsymbol{D}}$ using Eq. (B20).
2. Solve Eq. (B21) for $\Delta^{\theta}_{tt}\underline{\boldsymbol{D}}$.
3. Substitute $\Delta^{\theta}_{tt}\underline{\boldsymbol{D}}$ into Eqs. (B13) and (B14) to update temperature and surface pressure.
4. Substitute the newly obtained $\underline{\boldsymbol{T}}^{n+1}$ and p_s^{n+1} into Eq. (B12) to get the normal velocity at the new time step.
5. Apply Asselin filter to v_n, T and p_s.
6. Switch time indices: $n-1 \leftarrow n$, $n \leftarrow n+1$, then go to step 1.

Appendix C

Normalized wavenumber-prequency diagrams of the aqua-planet simulations

See Fig. C1.

Acknowledgements. The authors are indebted to Almut Gassmann (now at IAP-Kühlungsborn), Christiane Jablonowski (University of Michigan), David Williamson (NCAR), Frank Giraldo (Naval Postgraduate School), Rupert Klein (Freie Universität Berlin), Hans-Joachim Herzog (German Weather Service), and Werner Bauer (MPI-M) for valuable and inspiring discussions. Hui Wan was recipient of a PhD fellowship from the ZEIT Foundation

"Ebelin and Gerd Bucerius" through their support to the International Max Planck Research School on Earth System Modelling. Preparation of this manuscript was partially supported by the Linus Pauling Distinguished Postdoctoral Fellowship of the Pacific Northwest National Laboratory, a multiprogram national laboratory operated by Battelle for the US Department of Energy. The computing resources used in this work were provided by the German Climate Computing Center (Deutsches Klimarechenzentrum, DKRZ).

The service charges for this open access publication
have been covered by the Max Planck Society.

References

Asselin, F.: Frequency filter for time integrations, Mon. Weather Rev., 100, 487–490, 1972. 78

Bonaventura, L. and Ringler, T.: Analysis of discrete shallow water models on geodesic Delaunay grids with C-type staggering, Mon. Weather Rev., 133, 2351–2373, 2005. 61, 64, 89

Bonaventura, L., Iske, A., and Miglio, E.: Kernel-based vector field reconstruction in computational fluid dynamic models, Int. J. Numer. Meth. Fl., 66, 714–729, 2011. 74

Bonaventura, L., Redler, R., and Budich, R.: Earth System Modelling – Volume 2: Algorithms, Code Infrastructure and Optimisation, Springer Verlag, doi:10.1007/978-3-642-23831-4, 2012. 61

Danilov, S.: On utility of triangular C-grid type discretization for numerical modeling of large-scale ocean flows, Ocean Dynam., 60, 1361–1369, 2010. 66, 67, 90

Gassmann, A.: Inspection of hexagonal and triangular C-grid discretizations of the shallow water equations, J. Comput. Phys., 230, 2706–2721, 2011. 67

Gassmann, A.: A global hexagonal C-grid non-hydrostatic dynamical core (ICON-IAP) designed for energetic consistency, Q. J. Roy. Meteor. Soc., doi:10.1002/qj.1960, 2012. 78

Gassmann, A.: Nonhydrostatic modelling with ICON, in: Workshop on Nonhydrostatic Modelling, European Centre for Medium-Range Weather Forecast, Reading, UK, 2010. 83

Giorgetta, M. A., Roeckner, E., Mauritsen, T., Bader, B. S. J., Crueger, T., Esch, M., Rast, S., Schmidt, L. K. H., Kinne, S., Möbis, B., and Krismer, T.: The Atmospheric General Circulation Model ECHAM6: Model Description, Tech. rep., MPI-M, Hamburg, Germany, 2012. 62, 87

Giraldo, F. X. and Rosmond, T. E.: A scalable spectral element Eulerian atmospheric model (SEE-AM) for NWP: dynamical core tests, Mon. Weather Rev., 132, 133–153, 2004. 61

Gross, E., Bonaventura, L., and Rosatti, G.: Consistency with continuity in conservative advection schemes for free-surface models, Int. J. Numer. Meth. Fl., 38, 307–327, 2002. 70

Heikes, R. and Randall, D. A.: Numerical integration of the shallow-water equations on a twisted icosahedral grid. Part I: Basic design and results of tests., Mon. Weather Rev., 123, 1862–1880, 1995. 61

Held, I. M. and Suarez, M. J.: A proposal for the intercomparison of the dynamical cores of atmospheric general circulation models, B. Am. Meteorol. Soc., 73, 1825–1830, 1994. 85, 86, 90

Hollingsworth, A., Kallberg, P. K., Renner, V., and Burridge, D. M.: An internal symmetric computational instability, Q. J. Roy. Meteor. Soc., 109, 417–428, 1983. 78

Jablonowski, C.: Test of the Dynamics of Two Global Weather Prediction Models of the German Weather Service: The Held-Suarez Test, Diploma thesis (in german), Metorological Institute of the University of Bonn, Germany, 1998. 86

Jablonowski, C. and Williamson, D. L.: A baroclinic instability test case for atmospheric model dynamical cores, Q. J. Roy. Meteor. Soc., 132, 2943–2975, 2006a. 80, 90, 109, 110, 111, 112

Jablonowski, C. and Williamson, D. L.: A Baroclinic Wave Test Case for Dynamical Cores of General Circulation Models: Model Intercomparisions, NCAR Technical Note NCAR/TN-469+STR, NCAR, 2006b. 80, 90, 109, 110, 111, 112

Jöckel, P., von Kuhlmann, R., Lawrence, M. G., Steil, B., Brenninkmeijer, C. A. M., Crutzen, P. J., Rasch, P. J., and Eaton, B.: On a fundamental problem in implementing flux-form advection schemes for tracer transport in 3-dimensional general circulation and chemistry transport models., Q. J. Roy. Meteor. Soc., 127, 1035–1052, doi:10.1002/qj.49712757318, 2001. 70

Le Roux, D. Y., Rostand, V., and Pouliot, B.: Analysis of numerically induced oscillations in 2-D finite-element shallow water models. Part I: Inertia-gravity waves, SIAM J. Sci. Comput., 29, 331–360, 2007. 66, 90

Lin, S.-J.: A “vertically Lagrangian” finite-volume dynamical core for global models, Mon. Weather Rev., 132, 2293–2307, 2004. 72, 83, 86

Lin, S. J. and Rood, R. B.: Multidimensional flux-form semi-Lagrangian transport schemes, Mon. Weather Rev., 124, 2046–2070, doi:10.1175/1520-0493(1996)124<2046:MFFSLT>2.0.CO;2, 1996. 70

Lorenz, E. N.: Energy and numerical weather prediction, Tellus, 12, 364–373, 1960. 65

Majewski, D., Liermann, D., Prohl, P., Ritter, B., Buchhold, M., Hanisch, T., Paul, G., Wergen, W., and Baumgardner, J.: The operational global icosahedral-hexagonal gridpoint model GME: description and high resolution tests, Mon. Weather Rev., 130, 319–338, 2002. 61, 79

Narcowich, F. and Ward, J.: Generalized Hermite interpolation via matrix-valued conditionally positive definite functions, Math. Comput., 63, 661–687, 1994. 74

Neale, R. B. and Hoskins, B. J.: A standard test for AGCMs including their physical parameterizations. I: The proposal, Atmos. Sci. Lett., 1, 101–107, 2000. 87, 88, 90

Ničković, S., Gavrilov, M. B., and Tošić, I. A.: Geostrophic adjustment on hexagonal grids, Mon. Weather Rev., 130, 668–683, 2002. 66

Press, W. H., Teukolsky, S. A., Vetterling, W. T., and Flannery, B. P.: Numerical Recipes in Fortran 77: The Art of Scientific Computing, 2nd edn., Cambridge University Press,, 1992. 86

Ringler, T. and Randall, D.: The ZM grid: an alternative to the Z grid, Mon. Weather Rev., 130, 1411–1422, 2002. 61

Rípodas, P., Gassmann, A., Förstner, J., Majewski, D., Giorgetta, M., Korn, P., Kornblueh, L., Wan, H., Zängl, G., Bonaventura, L., and Heinze, T.: Icosahedral Shallow Water Model (ICOSWM): results of shallow water test cases and sensitivity to model parameters, Geosci. Model Dev., 2, 231–251, doi:10.5194/gmd-2-231-2009, 2009. 61, 70, 72, 90

Roeckner, E., Arpe, K., Bengtsson, L., Brinkop, S., Dümenil, L., Esch, M., Kirk, E., Lunkeit, F., Ponater, M., Rockel, B., Sausen, R., Schleese, U., Schubert, S., and Windelband, M.: Simulation of the Present-Day Climate With the ECHAM Model: Impact of Model Physics and Resolution, Technical Report 93, Max Planck Institute for Meteorology, 1992. 62

Roeckner, E., Arpe, K., Bengtsson, L., Christoph, M., Claussen, M., Dümenil, L., Esch, M., Giorgetta, M., Schlese, U., and Schulzweida, U.: The Atmospheric General Circulation Model ECHAM-4: Model Description and Simulation of Present-Day Climate, Technical Report 218, Max Planck Institute for Meteorology, 1996. 62

Roeckner, E., Bäuml, G., Bonaventura, L., Brokopf, R., Esch, M., Giorgetta, M., Hagemann, S., Kirchner, I., Kornblueh, L., Manzini, E., Rhodin, A., Schlese, U., Schulzweida, U., and Tompkins, A.: The Atmospheric General Circulation Model ECHAM5. PART I: Model Description, Technical Report 349, Max Planck Institute for Meteorology, 2003. 74

Roeckner, E., Brokopf, R., Esch, M., Giorgetta, M., Hagemann, S., Kornblueh, L., Manzini, E., Schlese, U., and Schulzweida, U.: Sensitivity of simulated climate to horizontal and vertical resolution in the ECHAM5 atmosphere model, J. Climate, 19, 3771–3791, 2006. 62, 65, 79

Ruppert, T.: Vector Field Reconstruction by Radial Basis Functions, Diploma thesis, Department of Mathematics, Technical University Darmstadt, Germany, 2007. 74

Saad, Y. and Schultz, M. H.: GMRES: a generalized minimal residual algorithm for solving nonsymmetric linear systems, SIAM J. Sci. Stat. Comp., 7, 856–859, 1986. 79

Sadourny, R., Arakawa, A., and Mintz, Y.: Integration of the nondivergent barotropic vorticity equation with a icosahedral-hexagonal grid for the sphere, Mon. Weather Rev., 96, 351–356, 1968. 61, 64

Simmons, A. J. and Burridge, D. M.: An energy and angular-momentum conserving vertical finite difference scheme and hybrid vertical coordinates, Mon. Weather Rev., 109, 758–766, 1981. 76, 90, 95

Simmons, A. J. and Strüfing, R.: An Energy and Angular-Momentum Conservinq Finite Difference Scheme, Hybrid Coordinates and Medium-Range Weather Prediction, Technical Report 28, ECMWF, Reading, UK, 1981. 64, 74

Skamarock, W. C. and Gassmann, A.: Conservative transport schemes for spherical geodesic grids: high-order flux operators for ODE-based time integration, Mon. Weather Rev., 139, 2962–2975, 2011. 83

Skamarock, W. C., Ringler, T., Thuburn, J., and Klemp, J.: Global nonhydrostatic modeling using Voronoi meshes: the MPAS model, in: Workshop on Nonhydrostatic Modelling, European Centre for Medium-Range Weather Forecast, Reading, UK, 2010. 83

Thuburn, J.: Numerical wave propagation on the hexagonal C-grid, J. Comput. Phys., 227, 5836–5858, 2008. 66

Thuburn, J., Ringler, T. D., Klemp, J. B., and Skamarock, W. C.: Numerical representation of geostrophic modes on arbitrarily structured C-grids, J. Comput. Phys., 228, 8321–8335, 2009. 66

Tomita, H. and Satoh, M.: A new dynamical framework of nonhydrostatic global model using the icosahedral grid, Fluid Dyn. Res., 34, 357–400, 2004. 61

Tomita, H., Tsugawa, M., Satoh, M., and Goto, K.: Shallow water model on a modified icosahedral grid by using spring dynamics, J. Comp. Phys., 174, 579–613, 2001. 64, 79

Wan, H.: Developing and testing a hydrostatic atmospheric dynamical core on triangular grids, Reports on Earth System Science 65, PhD thesis, MPI-M, Hamburg, Germany, 2009. 69, 79

Wan, H., Giorgetta, M. A., and Bonaventura, L.: Ensemble Held-Suarez test with a spectral transform model: variability, sensitivity, and convergence, Mon. Weather Rev., 136, 1075–1092, 2008. 85, 86

Wheeler, M. C. and Kiladis, G. N.: Convectively coupled equatorial waves: analysis of clouds and temperature in the wavenumber-frequency domain, J. Atmos. Sci, 56, 374–399, 1999. 88, 118

Williamson, D. L.: Integration of the barotropic vorticity equation on a spherical geodesic grid, Tellus, 20, 642–653, 1968. 61

Williamson, D. L.: Equivalent finite volume and Eulerian spectral transform horizontal resolutions established from aqua-planet simulations, Tellus A, 60, 839–847, 2008. 88, 89

Williamson, D. L., Drake, J. B., Hack, J. J., Jakob, R., and Swarztrauber, R. N.: A standard test set for numerical approximations to the shallow water equations in spherical geometry, J. Comput. Phys., 102, 221–224, 1992. 79

Williamson, D. L., Blackburn, M., Hoskins, B. J., Nakajima, K., Ohfuchi, W., Takahashi, Y. O., Hayashi, Y.-Y., Ishiwatari, H. N. M., McGregor, J., Borth, H., Wirth, V., Frank, H., Bechtold, P., Wedi, N. P., Tomita, H., Satoh, M., Zhao, M., Held, I. M., Suarez, M. J., Lee, M.-I., Watanabe, M., Kimoto, M., Liu, Y., Wang, Z., Molod, A., Rajendran, K., Kitoh, A., and Stratton, R.: The APE Atlas, NCAR Technical Note NCAR/TN-484+STR, National Center for Atmospheric Research, Boulder, CO, USA, 2011. 88, 89

Zhang, K., Wan, H., Wang, B., and Zhang, M. G.: Consistency problem with tracer advection in the atmospheric model GAMIL, Adv. Atmos. Sci., 25, 306–318, doi:10.1007/s00376-008-0306-z, 2008. 70

Table 1. Total number of triangle cells and edges in various grids with root division $n_r = 2$, the average distance between neighboring cells, and the area ratio of largest to smallest triangles. Grid −1 is the icosahedron projected onto the sphere.

Grid	Number of triangular cells	Number of triangle edges	Average distance between cell centers	Max : min cell area ratio
−1	20	30	4431.0 km	1.00
R2B0	80	120	2215.5 km	1.20
R2B1	320	480	1107.8 km	1.20
R2B2	1280	1920	553.9 km	1.27
R2B3	5120	7680	276.9 km	1.32
R2B4	20 480	30 720	138.4 km	1.38
R2B5	81 920	122 880	69.2 km	1.44
R2B6	327 680	491 520	34.6 km	1.49
R2B7	1 310 720	1 966 080	17.3 km	1.53

Table 2. Resolutions of the ICOHDC and the spectral core of ECHAM that produce similar results in the baroclinic wave test case. The degrees of freedom (DOF) of the ICOHDC are defined as the total number of velocity and mass (temperature) points on one vertical level; Those of the spectral core are defined as the total number of spectral coefficients of vorticity, divergence, and temperature on one vertical level. n_M stands for the total number of mass points, again on one vertical level. The n_M in the spectral model is that of the corresponding Gauss grid. "dx" in the right half of the table refers to the zonal spacing of the Gauss grid.

ICOHDC				Spectral core of ECHAM				
Grid Name	Grid Size	DOF	n_M	Truncation	dx at 60° N	dx at Equator	DOF	n_M
R2B4	138.5 km	51 200	20 480	(T51)	130.0 km	260.0 km	8268	11 858
R5B3	110.8 km	80 000	32 000	T63	105.3 km	210.7 km	12 480	18 050
R3B4	92.3 km	115 200	46 080	(T76)	87.0 km	174.1 km	18 018	26 450
R2B5	69.2 km	204 800	81 920	T106	62.6 km	125.1 km	34 668	51 200
R5B4	55.4 km	320 000	128 000	T127	52.4 km	104.8 km	49 536	72 962
R3B5	46.2 km	460 800	184 320	(T151)	44.1 km	88.2 km	69 768	103 058
R2B6	34.6 km	819 200	327 680	(T213)	31.3 km	62.5 km	138 030	204 800
R5B5	27.7 km	1 280 000	512 000	T255	26.1 km	52.3 km	197 376	293 378
R3B6	23.1 km	1 843 200	737 280	(T302)	22.0 km	44.1 km	276 336	412 232
R2B7	17.3 km	3 276 800	1 310 720	(T403)	16.5 km	33.1 km	490 860	732 050

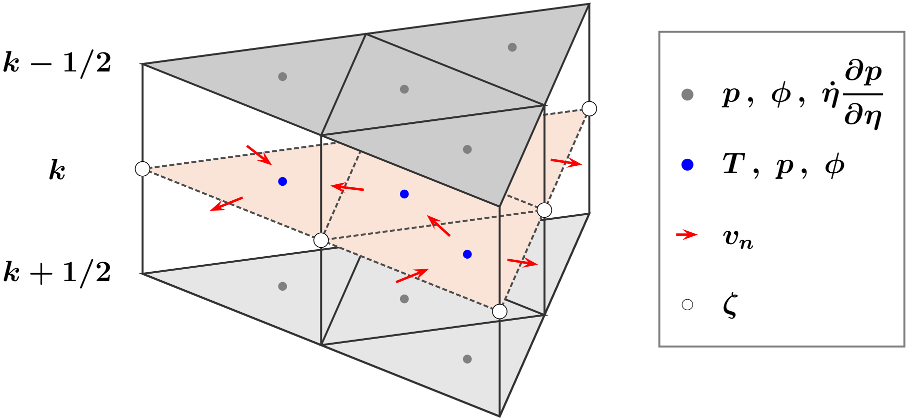

Fig. 1. Illustration of the triangular grid and the location of main variables. Vertical level indices are shown to the left of the sketch. The meaning of the symbols can be found in Sects. 2 and 3.

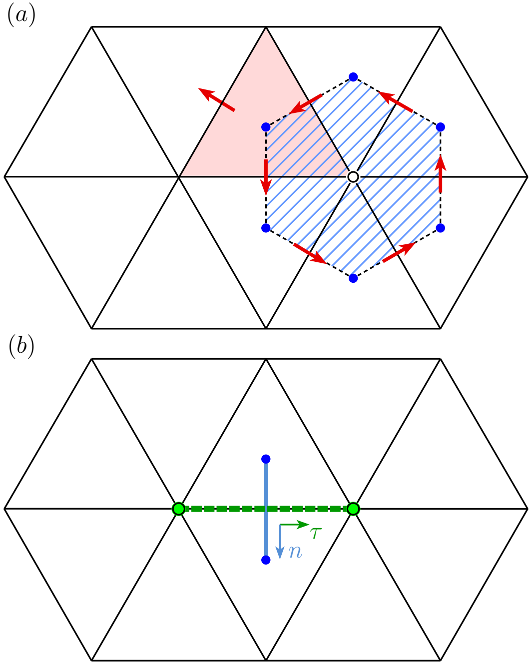

Fig. 2. Schematic showing the stencils of **(a)** the divergence and curl operators, and **(b)** the normal and tangential gradient operators described in Sect. 4.1.

GMDD
6, 59–119, 2013
A dynamical core on triangular grids – Part 1
H. Wan et al.

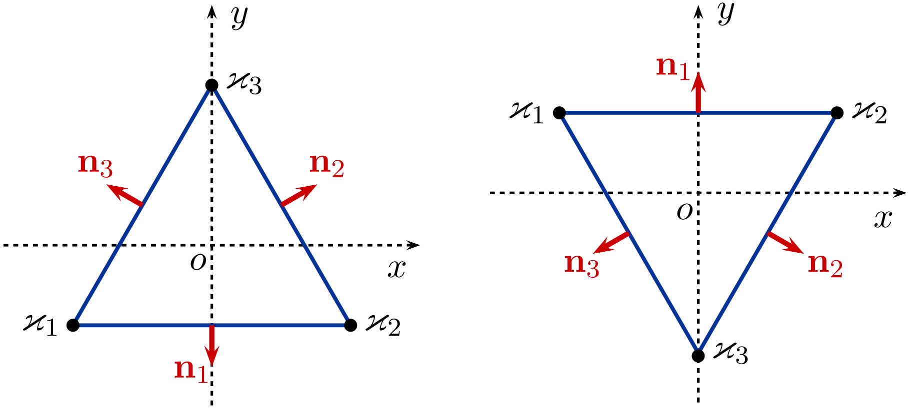

$\delta = 0$ $\delta = 1$

Fig. 3. Planar equilateral triangles considered in the truncation error analysis in Sect. 4.2.

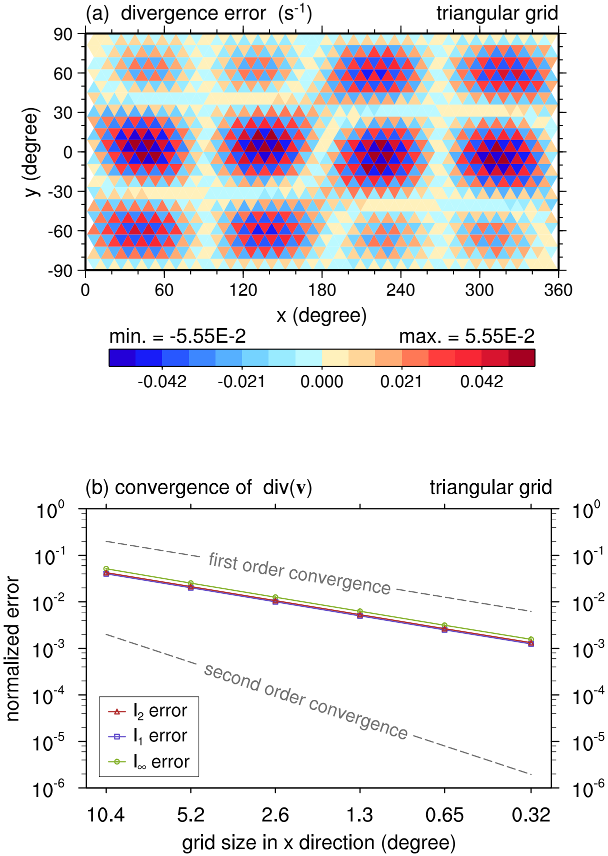

Fig. 4. **(a)** Numerical error of the cell-averaged divergence of the velocity field defined by Eq. (11), calculated using Eq. (6) on a planar triangular grid with 10.4° resolution in the x-direction. **(b)** The l_1, l_2 and l_∞ error norms at different resolutions. The discrete divergence is calculated by first evaluating Eq. (11) at edge centers then applying operator (6). Numerical error is computed with respect to cell average.

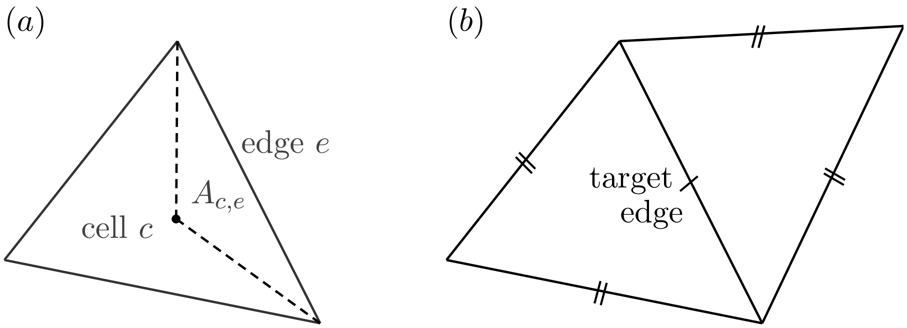

Fig. 5. (a) Schematic for the area-weighted averaging defined by Eq. (21); **(b)** stencil of the vector reconstruction used for obtaining the tangential velocity in Eqs. (22) and (23).

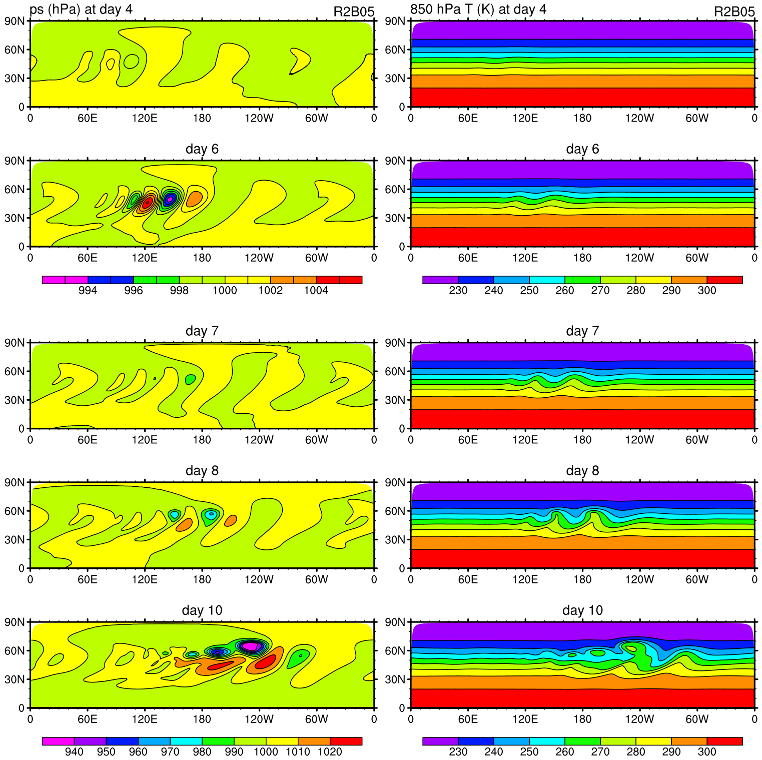

Fig. 6. Evolution of the baroclinic wave in the Jablonowski and Williamson (2006a,b) test case, as shown by the surface pressure (unit: hPa, left column) and 850 hPa temperature (unit: K, right column) simulated by the new dynamical core at R2B5 (70 km) resolution. Further details can be found in Sect. 6.1.2.

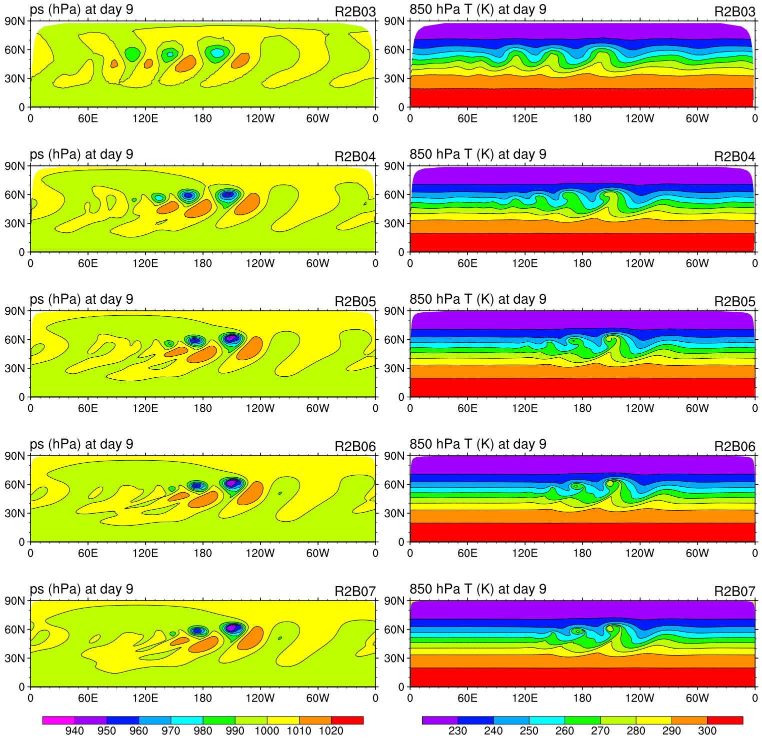

Fig. 7. Surface pressure (unit: hPa, left column) and 850 hPa temperature (unit: K, right column) at day 9 in the Jablonowski and Williamson (2006a,b) baroclinic wave test simulated by the new dynamical core at various horizontal resolutions. Further details can be found in Sect. 6.1.2.

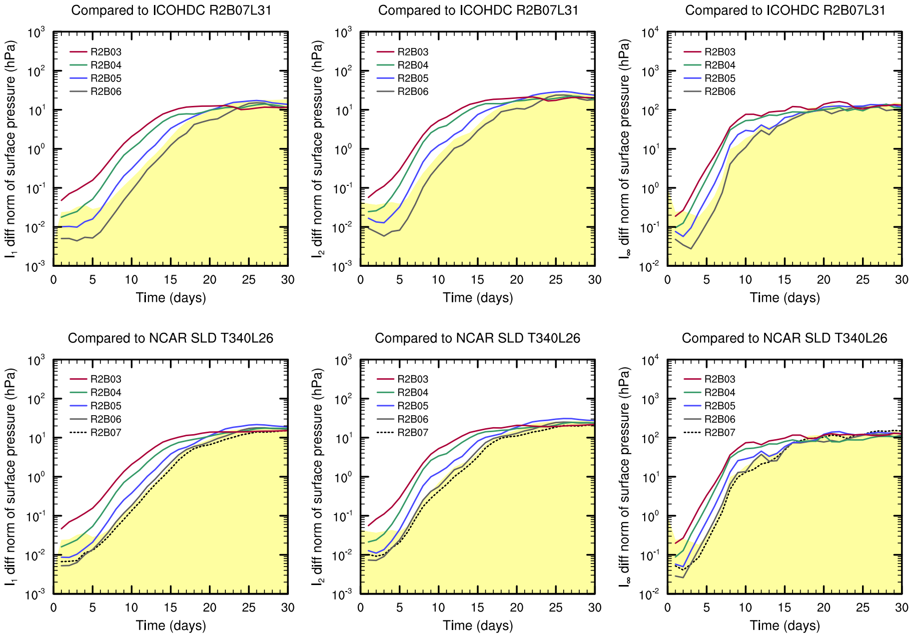

Fig. 8. l_1, l_2 and l_∞ norms (left, middle and right columns, respectively) of surface pressure differences (unit: hPa) in the Jablonowski and Williamson (2006a,b) baroclinic wave test between lower-resolution ICOHDC simulations and the R2B7 solution (upper row), and between all ICOHDC simulations shown in Fig. 7 and the NCAR semi-Lagrangian model result at T340 resolution (lower row). Further details can be found in Sect. 6.1.2.

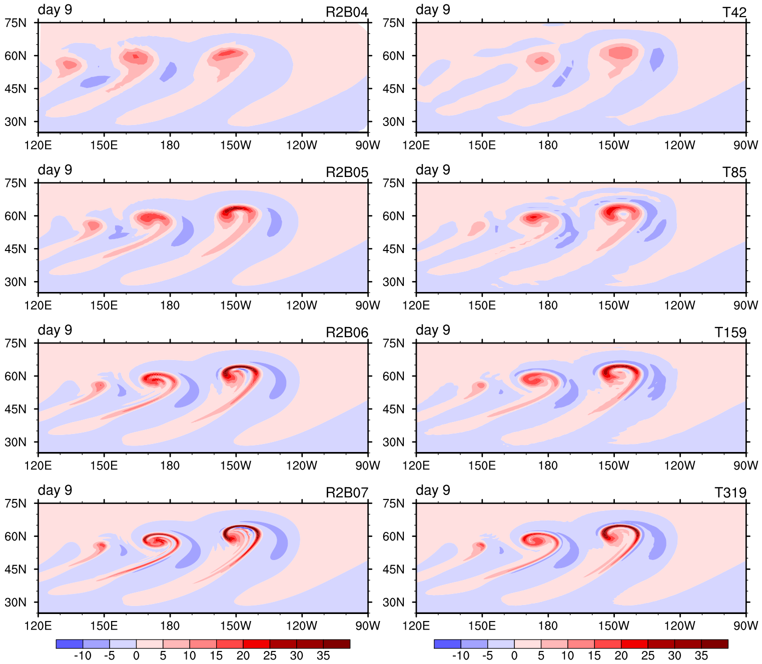

Fig. 9. 850 hPa relative vorticity (unit: $10^{-6}\,s^{-1}$) at day 9 in the Jablonowski and Williamson (2006a,b) baroclinic instability test simulated by the new dynamical core (left column) and the spectral transform core of ECHAM (right column) at various horizontal resolutions. Further details can be found in Sect. 6.1.2.

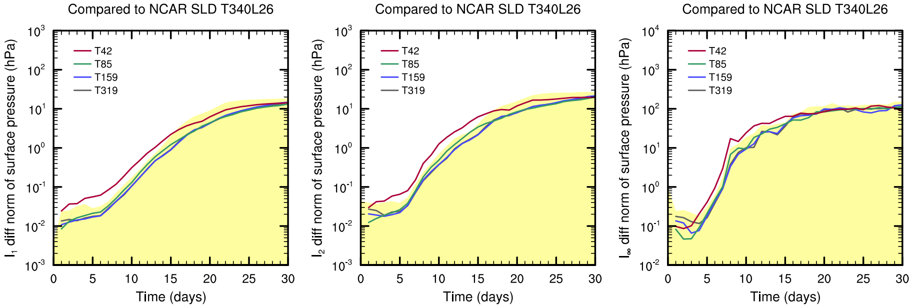

Fig. 10. As in Fig. 8 but between simulations performed with the spectral transform dynamical core of ECHAM and the reference solution at T340 provided by the NCAR semi-Lagrangian model.

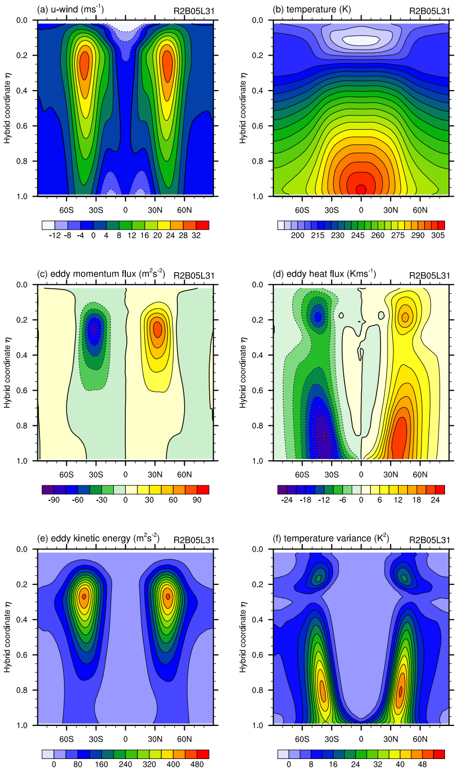

Fig. 11. Zonal mean climate state simulated by the ICOHDC in the Held-Suarez test at R2B5 resolution. The quantities shown are ensemble averages of 10 independent integrations. Each ensemble member starts from the same initial condition but with random noise added to the wind field. Further details can be found in Sect. 6.2.

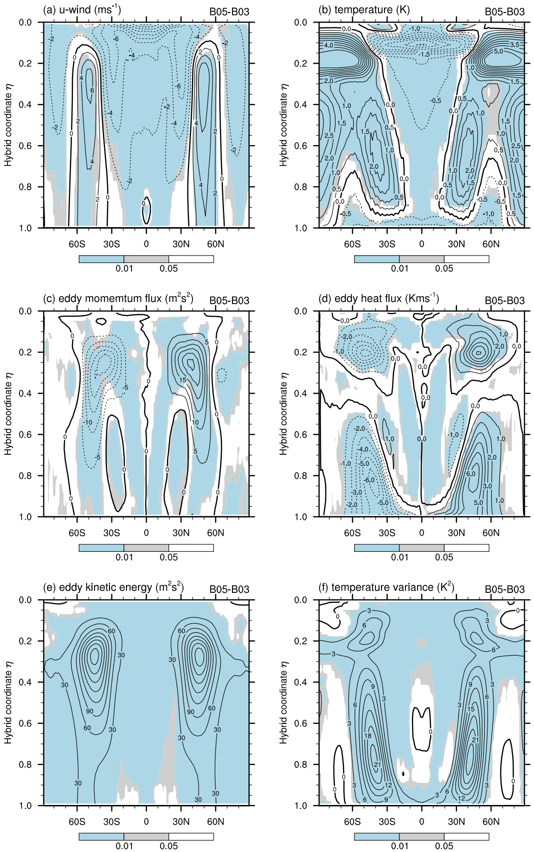

Fig. 12. Differences between the ensemble mean climate statistics in the Held-Suarez tests performed with the ICOHDC at R2B3 and R2B5 resolutions. Dashed contours indicate negative values. In the areas with gray and light blue shading, the differences are judged to be significant in the Kolmogorov-Smirnov test at 0.05 and 0.01 significance levels, respectively. Further details can be found in Sect. 6.2.

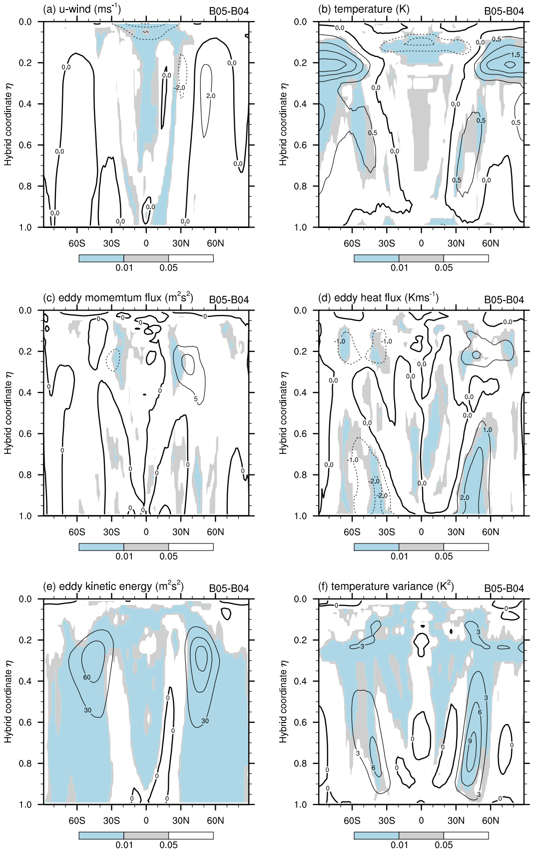

Fig. 13. As in Fig. 12 but for the differences between R2B4 and R2B5 simulations.

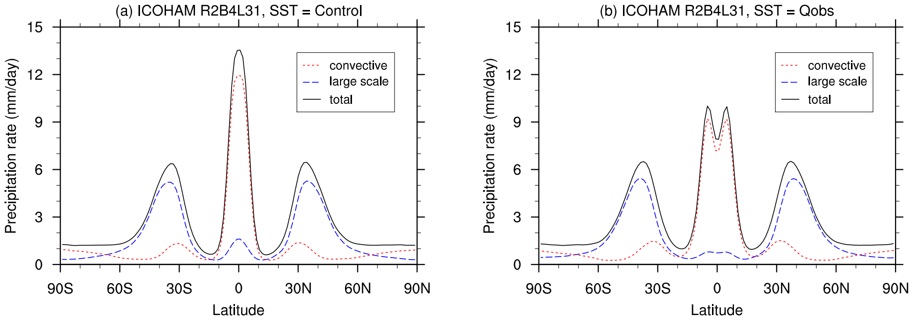

Fig. 14. Time and zonal mean surface precipitation rate (unit: mm day^{-1}, solid black lines) simulated by ICOHAM in aqua-planet simulations at R2B4L31 resolution using the "Control" (left) and "Qobs" (right) SST profiles. The contributions from convective (dotted red lines) and large-scale (dashed blue lines) precipitation are also displayed. Further details can be found in Sect. 7.

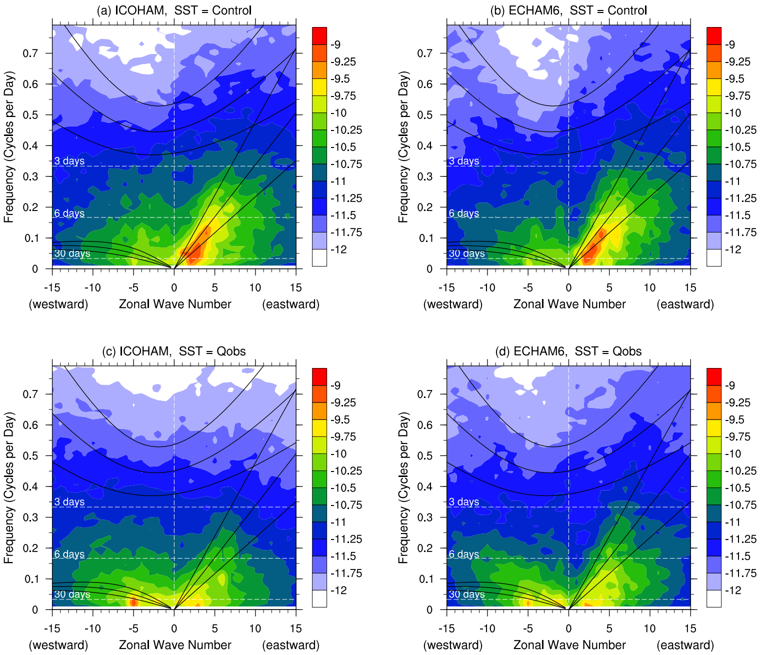

Fig. 15. Wavenumber-frequency diagrams of tropical precipitation (meridionally averaged between 10° S–10° N) in aqua-planet simulations carried out with ICOHAM at R2B4L31 (left column) and ECHAM6 at T63L47 (right column). The color shading shows the logarithm of the power of the symmetric component of the unnormalized spectra, diagnosed using the methodology of Wheeler and Kiladis (1999). The black lines indicate the dispersion relationships of westward propagating equatorial Rossby waves, eastward propagating Kelvin waves, and inertia-gravity waves that can propagate either westward or eastward. The upper row shows results corresponding to the "Control" SST profile. The lower row correspond to the "Qobs" profile. Further details can be found in Sect. 7.

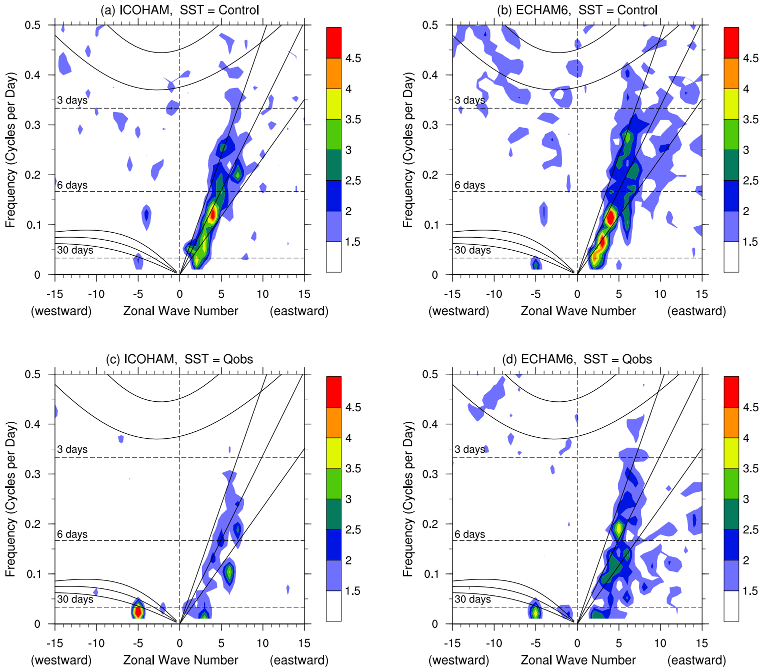

Fig. C1. As in Fig. 15 but showing the normalized spectra. Further details can be found in Sect. 7.